

Machine learning of quantum data using optimal similarity measurements

Zhenghao Li,^{1,*} Hao Zhan,^{1,2,*} Shana H. Winston,¹ Ewan Mer,¹ Zhenghao Yin,³ Shang Yu,^{1,4} Yazeed K. Alwehaibi,¹ Gerard J. Machado,^{1,5} Dayne Marcus Lopena,^{1,4} Lijian Zhang,² M. S. Kim,^{1,4,†} Aonan Zhang,^{1,5,‡} Ian A. Walmsley,^{1,4,5,§} and Raj B. Patel^{1,4,¶}

¹*Department of Physics, Imperial College London, Prince Consort Road, London, SW7 2AZ, UK*

²*College of Engineering and Applied Sciences, Nanjing University, 163 Xianlin Road, Nanjing 210093, China*

³*University of Vienna, Faculty of Physics, Vienna Center for Quantum*

Science and Technology (VCQ), Boltzmanngasse 5, Vienna A-1090, Austria

⁴*Centre for Quantum Engineering, Science and Technology (QuEST), Imperial College London, Prince Consort Rd, London, SW7 2AZ, United Kingdom*

⁵*Clarendon Laboratory, University of Oxford, Parks Road, Oxford OX1 3PU, UK*

Quantum machine learning seeks a computational advantage in data processing by evaluating functions of quantum states, such as their similarity, that can be classically intractable to compute. For quantum advantage to be possible, however, it is essential to bypass costly characterisation of individual data instances in favour of efficient, direct similarity evaluation. Here we demonstrate a sample-optimal, hardware-efficient protocol for estimating quantum similarity – the state overlap – using bosonic quantum interference. The sample complexity of this approach is independent of the system dimension and is information-theoretically optimal up to a constant factor. Experimentally, we implement the scheme on *Prakash-1*, a quantum computing platform based on a fully programmable integrated photonic processor. By preparing and interfering qudit states on the chip to directly extract their overlap, we demonstrate classification and online learning of quantum data with high accuracy in realistic noisy experiments. Our results establish joint overlap measurements as a scalable pathway to efficient quantum data analysis and a practical building block for network-integrated quantum machine learning.

I. INTRODUCTION

Assessing the similarity between objects is an instinctive process fundamental to human cognition. Mirroring this, the computation of similarity drives modern machine learning [1, 2], and more recently, guides attention in transformer-based large language models through vector inner products [3, 4]. Quantum machine learning (QML) extends this concept to an exponentially large Hilbert space, where the overlap between two quantum states—the squared inner product between state vectors—plays the same organising role, serving, for instance, as the kernel function in quantum classifiers or the cost function in training quantum models (Fig. 1) [5–10]. Evaluating the quantum state overlap is a BQP-complete problem [11], which forms the computational foundation for potential quantum advantage in machine learning [12, 13].

Unlocking this quantum advantage relies on efficient measurement of similarities between quantum data at scale. Quantum mechanics enables direct processing of joint information between two unknown states, departing from the classical intuition that comparing objects first requires characterising them individually. The latter is challenging in emerging quantum networks, where

data are natively generated and transmitted as quantum states, such as the outputs of quantum simulators, processors, and sensors (Fig. 1a). While quantum kernels and variational learners have recently been implemented across various platforms [14–18], scaling up these protocols remains constrained by the unfavourable cost of overlap measurements. Protocols based on tomographic reconstruction or distributed measurements of individual data instances generally require a number of samples that grows exponentially with system size [19–21]. Alternative strategies attempt to bypass this complexity by encoding classical data into quantum circuits and concatenating one unitary with the inverse of another, but the experimental overhead of implementing deep unitaries becomes prohibitive at large scale [22]. Moreover, circuit-encoding methods require *a priori* knowledge of the classical description of the data, rendering them inapplicable to quantum-native data increasingly targeted by QML [23]. Direct sample- and hardware-efficient similarity evaluation becomes essential for scalable QML.

In this study, we establish a sample-optimal and scalable overlap estimation scheme for arbitrary photonic states based on bosonic quantum interference and photon-number parity readout. Unlike recent entanglement-assisted protocols, designed to learn individual quantum states or channels [24–27], our work exploits entangled measurements to directly learn the joint properties between two states. In addition to its experimental simplicity, the scheme provably achieves the optimal $O(\epsilon^{-2})$ sample complexity for an ϵ -additive error precision. The scaling is optimal up to a constant factor across all possible measurement strategies, even

* These authors contributed equally to this work.

† m.kim@imperial.ac.uk

‡ aonan.zhang@physics.ox.ac.uk

§ ian.walmsley@physics.ox.ac.uk

¶ raj.patel1@imperial.ac.uk

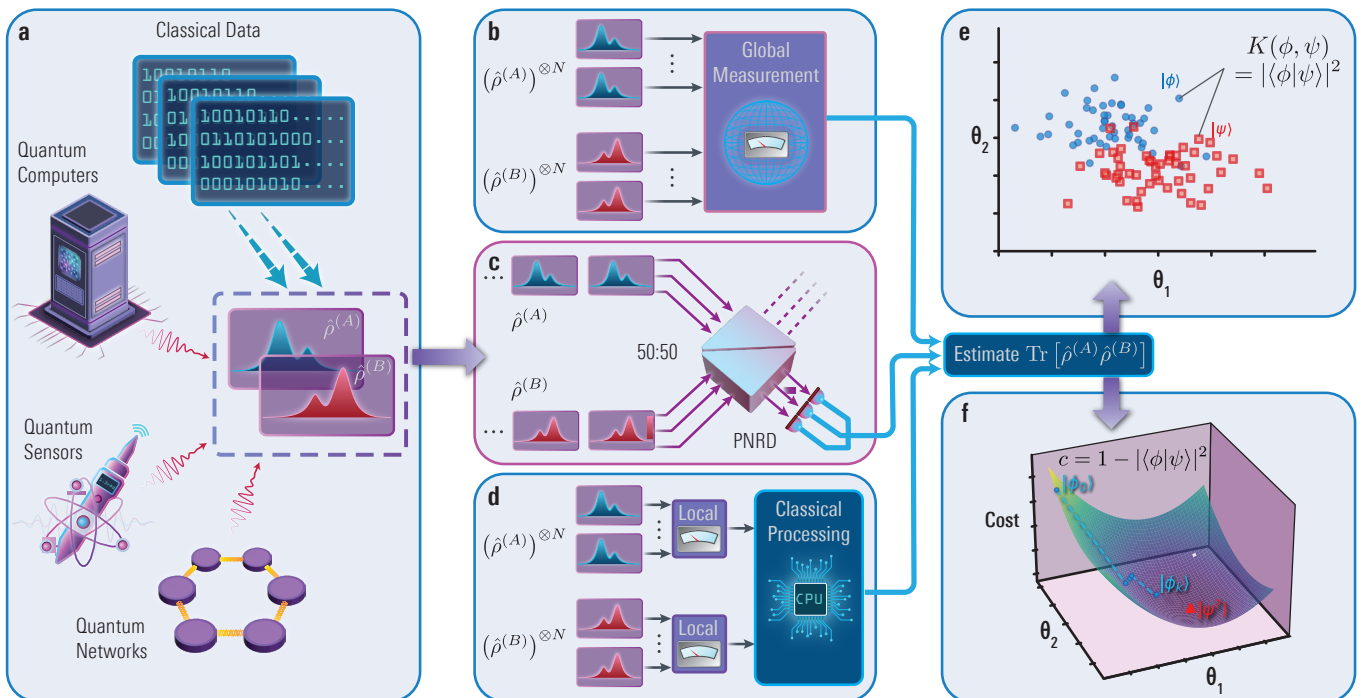


FIG. 1. Quantum machine learning (QML) with similarity measurements. (a) QML can process quantum states that encode classical data, though it also shows potential in learning native quantum data, such as the output states from fault-tolerant quantum computers, analogue quantum simulators, quantum sensors or information passed through large-scale quantum networks. A hierarchy of measurements exists to measure the similarity between two unknown quantum states via: (b) Global measurement on N copies of each state; (c) Sequential joint measurement using multi-mode bosonic interference on single copy of each state, derived and demonstrated in this work; (d) Distributed local measurements on N copies of each state separately followed by classical post-processing, an example of which we derive for CV states. Within this hierarchy, the interference-based joint measurement combines optimal sample complexity with experimental accessibility. For application in QML, we demonstrate the measurement as evaluation of (e) kernel functions for quantum data classification and (f) cost function for online learning. PNRD: photon-number-resolving detector.

when multi-copy global measurements are considered, whereas any distributed local measurement likely incurs an exponential cost. Crucially, the sample complexity is independent of the mode number, photon number or energy, thereby permitting scalable processing of high-dimensional quantum data.

Photons are ideal carriers of quantum data in future quantum networks, offering low decoherence, room-temperature operation, and compatibility with telecom infrastructure, along with the rich capability of encoding both discrete-variable (DV) states and continuous-variable (CV) states. In photonic systems, similarity measurements have been previously derived for single-mode Gaussian states by linear-optical interference and Wigner function estimation [28], and later for DV states using two-photon interference as ancilla-free SWAP tests [21, 29–31] with recent generalisation to CV states [32]. Building on these foundations, we show that bosonic interference provides a universal and hardware-native solution for measuring similarities between arbitrary multi-photon multi-mode states with optimal information-theoretic complexity, highlighting a hierarchy in information extraction where joint mea-

surements may have an exponential advantage over distributed strategies.

Experimentally, we validate the measurement scheme and its application to QML on *Prakash-1*, a photonic quantum computing platform with a fully programmable photonic integrated circuit (PIC) at its core, which implements a state-of-the-art compact rectangular decomposition of universal linear optics [33]. We prepare phase-encoded multi-mode qudit states and directly measure their overlap from the photon statistics. With experimentally estimated overlaps, we perform two QML tasks: classification of quantum datasets with over 90% accuracy and online learning of unknown target data with 98.3% median fidelity. Our results establish the joint overlap measurement via quantum interference as a hardware-efficient, sample-optimal enabler for scalable quantum data processing.

II. OVERLAP MEASUREMENT SCHEME

Photonic quantum data can be DV states, such as M -mode K -photon Fock states with Hilbert space dimen-

sion $d = \binom{M+K-1}{K}$, or CV states with theoretically infinite Hilbert space dimension that is only bounded by energy, including Gaussian states or non-Gaussian states such as Gottesman-Kitaev-Preskill (GKP) states [34]. We consider two general M -mode states $\hat{\rho}^{(A)}$ and $\hat{\rho}^{(B)}$ with their trace overlap given by $\text{Tr}[\hat{\rho}^{(A)}\hat{\rho}^{(B)}]$, which reduces to the squared overlap $|\langle\psi^{(A)}|\psi^{(B)}\rangle|^2$ for pure states $\hat{\rho}^{(A/B)} = |\psi^{(A/B)}\rangle\langle\psi^{(A/B)}|$.

Given N copies of each state, we consider three types of measurement schemes for estimating the overlap:

1. Global measurements on all $2N$ state copies, $(\hat{\rho}^{(A)} \otimes \hat{\rho}^{(B)})^{\otimes N}$;
2. Joint measurement via bosonic interference on only one copy of each state at a time, $(\hat{\rho}^{(A)} \otimes \hat{\rho}^{(B)})$;
3. Distributed measurements that perform local measurements on $(\hat{\rho}^{(A)})^{\otimes N}$ and $(\hat{\rho}^{(B)})^{\otimes N}$ respectively followed by post-processing of the outcomes.

The three measurement strategies are visualised in Fig. 1b-d. Both global and distributed schemes can allow arbitrary, adaptive, multi-round measurements.

Any M -mode photonic state can be described by $\hat{\rho} = \frac{1}{\pi^M} \int_{\mathbb{C}^M} d^{2M} \alpha \chi(\alpha) \hat{D}(-\alpha)$, where χ is its characteristic function and \hat{D} is the M -mode displacement operator. The overlap between two states, $\hat{\rho}^{(A/B)}$, is given by,

$$\text{Tr}[\hat{\rho}^{(A)}\hat{\rho}^{(B)}] = \frac{1}{\pi^M} \int_{\mathbb{C}^M} d^{2M} \alpha \chi^{(A)}(\alpha) \chi^{(B)}(-\alpha). \quad (1)$$

The two states, originating in registers labelled by A/B , are interfered on balanced beamsplitters (BSs). The BSs are described by a unitary operator \hat{U}_{BS} that combines the modes pairwise between the two registers: $\hat{U}_{\text{BS}}^\dagger \hat{a}_i^{(A)} \hat{U}_{\text{BS}} = \frac{1}{\sqrt{2}} (\hat{a}_i^{(A)} + \hat{a}_i^{(B)})$, $\hat{U}_{\text{BS}}^\dagger \hat{a}_i^{(B)} \hat{U}_{\text{BS}} = \frac{1}{\sqrt{2}} (\hat{a}_i^{(A)} - \hat{a}_i^{(B)})$, where the i -th mode in a register is labelled by subscript $i = 1, \dots, M$. We then measure the photon-number parity, $\hat{\Pi} = (-1)^{\sum_{i=1}^M \hat{n}_i^{(B)}}$, on output register B , where $\hat{n}_i^{(B)}$ is the photon number operator in the i -th mode. This gives a direct estimate of the two-state overlap:

$$\text{Tr}[\hat{\rho}^{(A)}\hat{\rho}^{(B)}] = \text{Tr}_{(B)} \left[\text{Tr}_{(A)} \left(\hat{U}_{\text{BS}}^\dagger \hat{\rho}^{(A)} \hat{\rho}^{(B)} \hat{U}_{\text{BS}} \right) \hat{\Pi} \right]. \quad (2)$$

The detailed derivation of Equation 2 is provided in Methods and Supplementary Information. While Equation 2 holds true for any general mixed states, we note that the trace overlap is a good measure of similarity when at least one of two states is pure.

Operationally, we can measure the output state using photon-number-resolving detectors (PNRDs). We sample N shots and record the number of even- and odd-total photon number events, from which we construct an unbiased overlap estimator. Using Hoeffding's bound, we can prove its sample complexity in Theorem 1 below.

Theorem 1. *Given N copies of $\hat{\rho}^{(A)} \otimes \hat{\rho}^{(B)}$ and use of balanced BSs and PNRDs, the overlap $\text{Tr}[\hat{\rho}^{(A)}\hat{\rho}^{(B)}]$ can be estimated to within additive error ϵ with success probability of at least $1 - \delta$ for sample complexity $N = O(\epsilon^{-2} \log(2\delta^{-1}))$.*

The sample complexity simplifies to $N = O(\epsilon^{-2})$ for a constant success probability $1 - \delta > 1/2$. The full proof is provided in the Supplementary Information. Importantly, the sample complexity is independent of the mode number, photon number, or energy, and requires only a single copy of each state per measurement. In the next section, we show that this performance is not only efficient, but also optimal within the full hierarchy of measurement strategies.

III. SAMPLE COMPLEXITY OPTIMALITY

The significance of the $O(\epsilon^{-2})$ scaling is best understood by comparing it to the fundamental limit and other measurement strategies of overlap estimation. Using Helstrom's bound [35], we can prove the following theorem.

Theorem 2. *Given the N -copy state, $(\rho^{(A)} \otimes \rho^{(B)})^{\otimes N}$, if an algorithm estimates $\text{Tr}[\rho^{(A)}\rho^{(B)}]$ to within additive error ϵ with success probability of at least $1 - \delta$, then $N = \Omega(\epsilon^{-2}(1 - 2\delta)^2/4)$.*

The proof of Theorem 2 is first given in Ref. [20] for the SWAP test in DV systems, which can be extended to arbitrary states, including CV states, with full proof provided in Supplementary Information. If given a constant success probability, such as $1 - \delta = 2/3$, Theorems 1 and 2 provide a tight bound of $N = \Theta(\epsilon^{-2})$, proving that the interference-based measurement is already optimal up to a constant scaling, even when considering experimentally more complex global measurements.

We also motivate the optimality of our scheme by considering the distributed overlap estimation problem [20] and argue that joint measurements likely have exponential advantage, as summarised in Table I. For the distributed problem, Alice and Bob are given $(\hat{\rho}^{(A/B)})^{\otimes N}$ respectively and are required to estimate their overlap by only local quantum operations and classical communication channels, but with adaptive, multi-round measurements allowed.

For DV states, any distributed approach scales exponentially with system size. Full tomographic reconstruction of at least one state requires a sample complexity of $O(d)$ [19], and distributed overlap estimation requires a sample complexity rigorously lower-bounded by $N = \Omega(\max(\epsilon^{-2}, \sqrt{d}\epsilon^{-1}))$ [20]. For an M -mode, K -photon state with Hilbert space dimension $d = \binom{M+K-1}{K}$, both complexities scale exponentially with the photon number and mode number.

For CV states with infinite density matrix dimension, it is often practical to assume some mode-extensive en-

TABLE I. Comparison of sample complexity for joint overlap estimation and distributed overlap estimation of discrete-variable (DV) states and continuous-variable (CV) states, respectively, to additive error ϵ and success probability $1 - \delta$. We summarise the information-theoretic lower bounds for comparison with the schemes derived in this work. Symbol d denotes dimension number of DV states, M mode number of photonic states. See main text and Methods for details.

		Joint overlap estimation on $(\hat{\rho}^{(A)} \otimes \hat{\rho}^{(B)})^{\otimes N}$	Distributed overlap estimation on $(\hat{\rho}^{(A)})^{\otimes N}, (\hat{\rho}^{(B)})^{\otimes N}$
Lower bound	DV states	$\Omega(\epsilon^{-2}(1 - 2\delta)^2/4)$ [20]	$\Omega(\max(\epsilon^{-2}, \sqrt{d}\epsilon^{-1}))$ [20]
	CV states	$\Omega(\epsilon^{-2}(1 - 2\delta)^2/4)$ ^a	Lower bound unknown
Our work	Any bosonic state	$O(\epsilon^{-2} \log(2\delta^{-1}))$	$\tilde{O}(\epsilon^{-4}(e\kappa)^{4M}/M^2)$ for self-reflective states ^b

^a Extended in our work to CV states from the proof of [20].

^b Logarithmic terms ignored in big- \tilde{O} notation for simplicity and κ is a mode-extensive energy bound.

ergy constraint, under which tomography is also inefficient with sample complexity being exponential in the mode number [36]. For distributed CV overlap estimation, no rigorous lower bound exists to the best of our knowledge. However, since energy bounded CV states can be approximated by truncated DV states [36], we conjecture that the CV problem suffers from a similar exponential lower bound as its DV counterpart.

To explicitly illustrate the curse of dimensionality, we consider a special class of self-reflective states, which include many experimentally interesting CV states such as coherent states, squeezed vacuum states, cat states and GKP states [37]. For these states, distributed learning of *individual* properties is ‘super-efficient’: Only constant sample complexity is required to estimate their characteristic functions for an exponential number of points in phase space [27, 37], which can then be used to estimate the overlap in Equation 1 by Monte-Carlo integration.

However, the overall sample complexity is still inefficient. For an M -mode CV state, we also assume a mode-extensive energy constraint κ , such that the phase-space integral in Equation 1 is negligible for $|\alpha| \geq \sqrt{\kappa M}$, thus defining a $2M$ -dimensional hypersphere in phase space. Even though we can efficiently estimate the characteristic functions of two states, a constant precision in overlap estimation requires the precision of $\chi^{(A/B)}(\alpha_i)$ at each point inside the hypersphere to scale inversely with the hypersphere volume, resulting in an overall sample complexity that remains exponential in M . We state the result informally in Theorem 3.

Theorem 3. (Informal.) *Given N copies of two M -mode self-reflective states, $\hat{\rho}^{(A)}, \hat{\rho}^{(B)}$, whose characteristic functions are limited within a phase-space hypersphere with radius $|\alpha| = \sqrt{\kappa M}$, the distributed overlap estimation problem can be solved with additive error ϵ and success probability of at least $2/3$ for sample complexity $N = \tilde{O}(\epsilon^{-4}(e\kappa)^{4M}/M^2)$.*

For notational simplicity, we drop logarithmic terms in the big- \tilde{O} notation from the already exponential complexity. The formal statement and full proof are given in the Supplementary Information.

IV. EXPERIMENTAL IMPLEMENTATION

We experimentally demonstrate the joint overlap estimation scheme with application to QML routines. Our experimental set-up relies on spontaneous parametric downconversion (SPDC) for preparing an indistinguishable photon pair at 1550 nm wavelength. The photon pair is produced by pumping a periodically-poled potassium titanyl phosphate (ppKTP) waveguide with 1 ps laser pulses at 775 nm wavelength.

A silicon nitride-based PIC implements a 10×10 square mesh of tunable phaseshifters as shown in Fig. 2, enabling universal linear optical operations. The PIC layout—designed in-house—implements a rectangular mesh of thermo-optic phaseshifters that can decompose arbitrary 10×10 unitary transformations following the Bell-scheme in Ref. [33]. The PIC is programmed to encode each photon into a qudit state that is a spatial superposition over four spatial modes with three tunable relative phases:

$$|\psi(\boldsymbol{\theta})\rangle = \left(A_0 \hat{a}_0^\dagger + \sum_{k=1}^3 A_k e^{i\theta_k} \hat{a}_k^\dagger \right) |0\rangle, \quad (3)$$

where \hat{a}_k^\dagger for $k \in [0, 3]$ are the bosonic creation operators for the four spatial modes and A_k are the real amplitudes. Vector $\boldsymbol{\theta} = [\theta_1, \theta_2, \theta_3]$ are the tunable parameters for either data encoding or model training.

The two qudits occupy eight modes in total, which we split into two registers. According to Equation 2, our general overlap estimation scheme requires four PNRDs on one of the registers. However, when the total photon number is at most two, an odd-parity measurement in one register is equivalent to a coincidence detection between the two registers, and the overlap is equal to one minus twice the probability of these coincidence events, $\langle \hat{\Pi} \rangle = 1 - 2P_{\text{odd}}$. Measurement in our experiment is performed by click-detection on all eight output modes by superconducting nanowire single-photon detectors (SNSPDs), which are non-photon-number-resolving detectors.

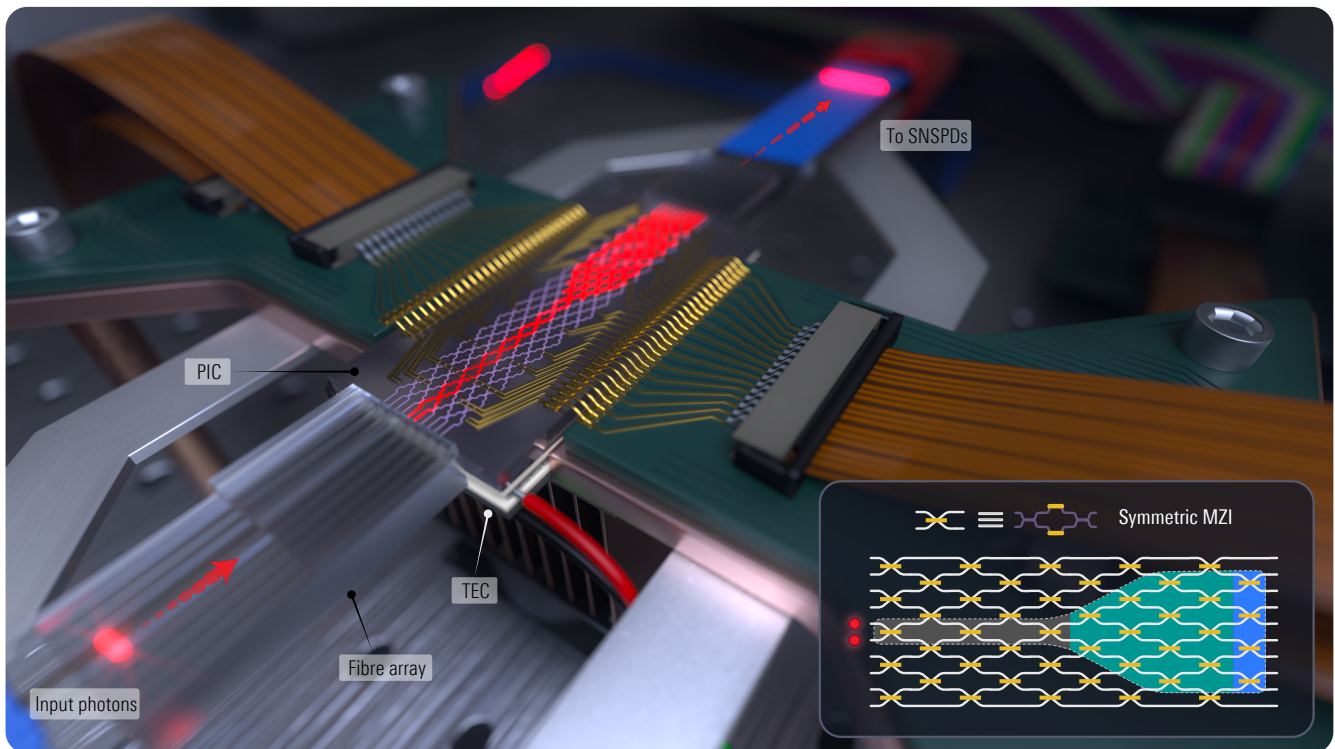


FIG. 2. An illustration of the fully-programmable Si_3N_4 integrated photonic processor at the heart of the quantum computing platform *Prakash-1*. A photonic integrated circuit (PIC), whose temperature is maintained by a thermo-electric cooling (TEC) unit, employs a square mesh of symmetric Mach-Zehnder interferometers (MZIs), with heating elements acting as thermo-optical phase shifters in each arm of the MZIs. Collectively, the MZIs plus ten stand-alone on-chip phase shifters (not used in this work and not shown) can implement an arbitrary 10×10 unitary transformation according to the Bell-scheme (see inset). The dashed line encloses the MZIs that are tuned in the experiment. The grey, teal, and blue areas indicate the MZIs used to route the photon pair, prepare the qudits, and perform the multi-mode interference, respectively. The output eight modes are fibre-coupled and routed to superconducting nanowire single-photon detectors (SNSPDs).

V. CLASSIFICATION OF QUANTUM DATA

To demonstrate the utility of the optimal similarity measurement, we first implement a supervised kernel-based classification routine on quantum data using overlap-based kernel evaluation. Kernel methods play a foundational role in statistical learning theory, offering nonlinear decision boundaries with strong generalisation guarantees. Notably, training sufficiently wide neural networks has been found to be equivalent to kernel regression with the neural tangent kernel [38].

In the quantum setting, kernel methods arise naturally: encoding data $\mathbf{x}^{(i)} \in \mathbb{R}^d$ into quantum states $|\psi(\mathbf{x}^{(i)})\rangle$ defines a quantum feature map from the real space to Hilbert space, and the associated quantum kernel is evaluated by the state overlap, $K(\mathbf{x}^{(i)}, \mathbf{x}^{(j)}) = |\langle \psi(\mathbf{x}^{(i)}) | \psi(\mathbf{x}^{(j)}) \rangle|^2$. The task is to assign binary labels on unseen data $|\psi(\mathbf{x})\rangle$. We consider a setting in which training and test data are in the form of quantum states $|\psi(\mathbf{x})\rangle$ and all kernel entries $K(\mathbf{x}^{(i)}, \mathbf{x}^{(j)})$ are evaluated experimentally via bosonic interference. Given a set of training data $\{|\psi(\mathbf{x}^{(i)})\rangle\}_{i=1}^m$, each with label $y^{(i)}$, a support vector machine (SVM) constructs a lin-

ear classifier in the induced feature space, which predicts $\hat{y}(\mathbf{x}) = \text{sign}(\sum_{i=1}^m \beta^{(i)} y^{(i)} K(\mathbf{x}, \mathbf{x}^{(i)}) + b)$ for unseen data, with coefficients $\{\beta^{(i)}, b\}$ determined during training [2] (see Methods for details).

In our implementation, we generate three labelled datasets of 200 quantum states. Three-dimensional parameters are encoded in the qudit phases in Equation 3, $\mathbf{x}^{(i)} = [\theta_1^{(i)}, \theta_2^{(i)}, \theta_3^{(i)}]$, as illustrated in Fig. 3a. The three datasets comprise linearly separable clusters, concentric spheres, and partially overlapping clusters in the original parameter space (Fig. 3). Each dataset is split randomly into 100 training and 100 test states. Using experimentally measured overlaps with $N = 10^3$ samples per kernel evaluation, we obtain test accuracies of 100% (separate), $98.47 \pm 0.71\%$ (spherical), and $91.65 \pm 2.15\%$ (overlapping), with uncertainties estimated by bootstrapping. The latter two datasets, which are not linearly separable in the original parameter space, become separable through the quantum kernel. While the datasets used here are not specifically designed to maximise the performance separation over classical algorithms [13, 17], the experiment demonstrates a scalable protocol for supervised learning in the Hilbert space using experimentally

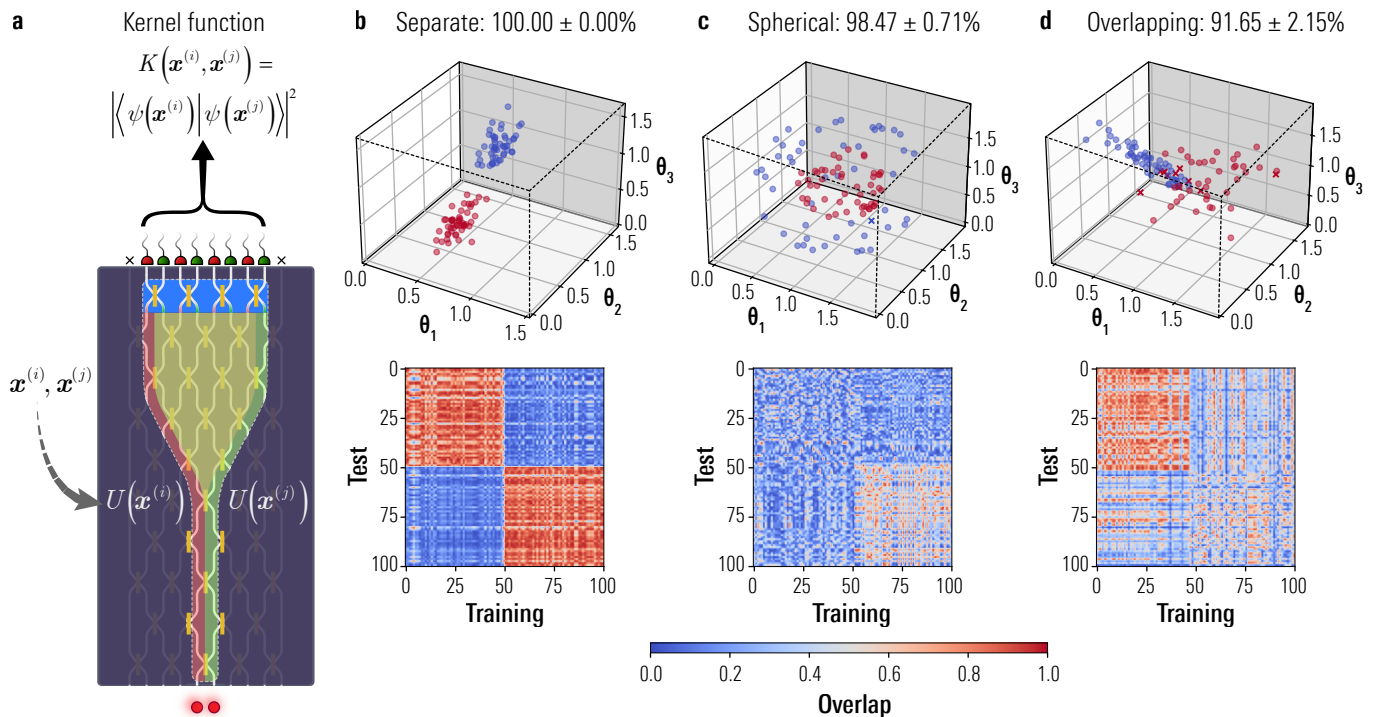


FIG. 3. Quantum data classification. (a) Schematic of experimental routine for kernel function evaluation. (b-d) Classification results for linearly separable data, spherically separable data and overlapping data respectively. The top panels visualise the test datasets. Each dataset contains 100 datapoints, which are three-dimensional vectors $\mathbf{x} = [\theta_1, \theta_2, \theta_3]$ represented by points in 3D space. The colour of each point indicates its groundtruth label, and is plotted with a circle marker if it is correctly classified, or a cross marker if it is misclassified. The bottom panels show the experimentally estimated overlap values (colour bar) between the test data and training data for each dataset. The datapoints are sorted by their labels for visualisation purposes.

realistic resources.

VI. ONLINE LEARNING OF QUANTUM DATA

In contrast to batch learning, online learning receives input data sequentially and processes them on the fly. For quantum data, online learning is often practical as it is difficult to prepare a large batch of identical state copies on noisy quantum hardware [39]. This scenario captures core tasks in QML, including training quantum neural networks [10] and implementing quantum generative models such as quantum generative adversarial networks [40], where a quantum model is trained to reproduce quantum data.

As a second application, we demonstrate overlap-based cost function evaluation in an online learning setting, where quantum data arrive sequentially as noisy copies of an unknown target state $|\psi(\mathbf{x}^{(t)})\rangle$. The objective is to train the output state $|\psi(\boldsymbol{\theta})\rangle$ of a parametrised quantum model with parameters $\boldsymbol{\theta}$ to approximate the target by minimising the infidelity $c(\boldsymbol{\theta}) = 1 - |\langle \psi(\mathbf{x}^{(t)}) | \psi(\boldsymbol{\theta}) \rangle|^2$. In each experiment, a randomly initialised qudit is prepared on chip as the target state, while a second independently tunable qudit serves as the output of the train-

able model. Parameters $\boldsymbol{\theta}$ are updated using simultaneous perturbation stochastic approximation (SPSA) [41], with gradients estimated from two overlap evaluations per iteration (Fig. 4a). This algorithm has been used in self-guided tomography for full state reconstruction, exhibiting superior efficiency and noise robustness compared to standard tomography methods [42–44]. Thermal crosstalk between phaseshifters induces fluctuations in target preparation, mimicking realistic hardware noise in which successive copies are not identical.

Despite this noise, the optimisation converges reliably. Across ten random targets, the infidelity decreases to the few-percent level within 500 iterations, with a median final value of 1.7×10^{-2} (Fig. 4b). At each iteration, the overlap evaluation consumes only $N = 10^2$ copies of the target state. Moreover, increasing N to 10^3 or 10^4 does not significantly change convergence rate or final precision, indicating robustness of the approach to shot noise. The convergence rate and final precision are in line with simulation results with a crosstalk noise model comparable with experimental parameters (see Supplementary Information for detailed results). Three representative optimisation trajectories in the three-dimensional parameter space of $\boldsymbol{\theta}$ are visualised in Fig. 4c. These results highlight the robustness of the cost-function evaluation

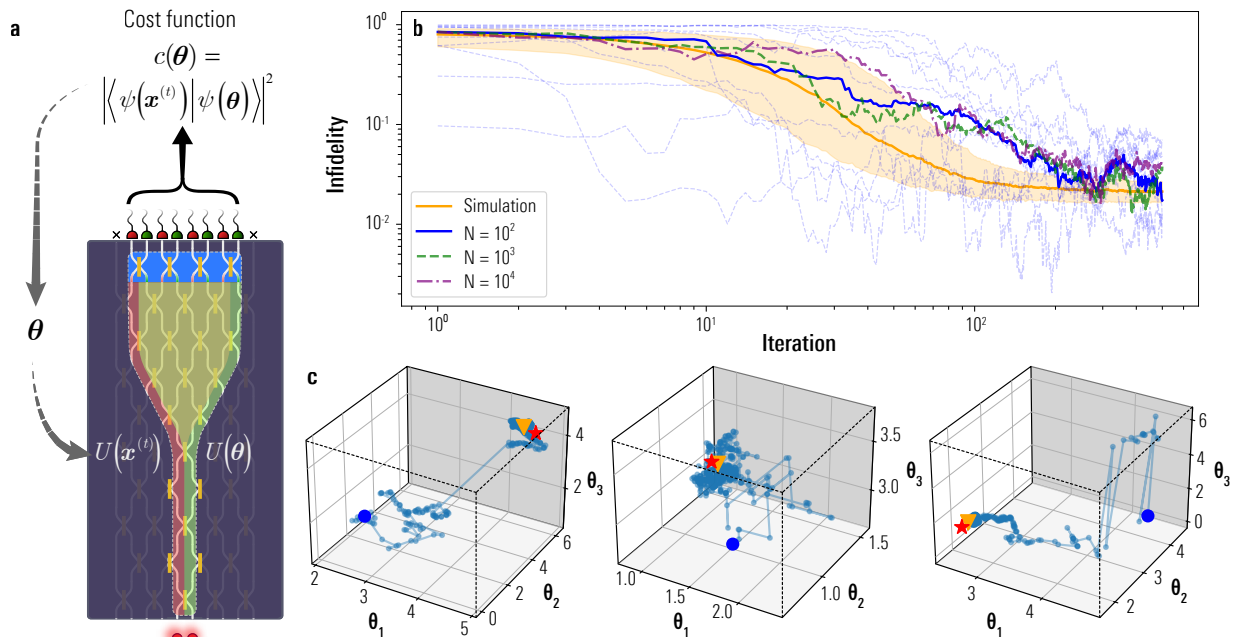


FIG. 4. Quantum data online learning. (a) Schematic of experimental routine for cost function evaluation. (b) Infidelity between the learned qudit state and the target qudit state against iteration number. Ten random target states are iteratively learned starting from random initial states, with $N = 10^2$ state copies used per overlap evaluation (light blue dashed lines). The median infidelity across the ten learning tasks is shown by the dark blue solid line. The experiment is repeated for different number of state copies per overlap evaluation, $N = 10^3$ and $N = 10^4$, with median performance shown in green and purple dashed lines respectively. The shaded regions indicate the interquartile range (i.e. between the 25% and 75% quantiles) across simulations over 500 randomised learning tasks, with median shown by the solid yellow line. (c) Optimisation paths for three example experiments in (b) with $N = 10^2$, visualised in the three-dimensional space of qudit phases. The red star markers plot the target point, the blue circle markers plot the initial point of each path, and the yellow triangle markers plot the optimal point found after 500 iterations.

and its suitability for learning from quantum data in realistic, noisy settings.

VII. DISCUSSION

In certain problems of structured data processing, QML has shown provable advantage over classical methods [12, 13, 17]. For efficient implementation, our optimal similarity measurement using bosonic interference achieves an exponential advantage over conventional methods that extract information about each state separately. In future quantum networks, where data are available naturally as quantum states, joint overlap estimation provides a minimal interface to extract relational information between quantum data, enabling applications such as distributed or blind quantum computing and learning [45, 46].

The experimental demonstrations of QML on the *Prakash-1* platform showcase the effectiveness of our approach in realistic, noisy experimental settings with modest quantum resources. For truly scalable QML, open questions of trainability in the form of barren plateaus or exponential concentration of kernel function values [47, 48] persist. Furthermore, the present imple-

mentation measures single-photon states evolved under linear-optical circuits, which have recently been shown to be classically simulable [49]. The seek for generalisable end-to-end advantages in QML remains an open frontier. Nevertheless, we demonstrate a sample-optimal overlap estimation that addresses the measurement part of the challenge. The scheme is equally applicable to photonic states with non-Gaussianity and high entanglement that are expected to be classically intractable [50–52]. Scaling up the scheme and integrating such complex states are the next steps for achieving quantum advantage.

For future work, extending the two-state interference to multi-state interference, which has been experimentally explored in photonic systems [53], could enable access to higher-order nonlinear functionals, expanding the expressive power of quantum models. Recent theoretical work has identified a hierarchy of learning capabilities enabled by increasing the number of jointly measured copies [54]. Higher-order functions between distinct quantum states could serve as the quantum analogue of multi-body attention mechanisms in transformer architectures, which potentially reduce hallucination and bias in generative artificial intelligence [55]. Looking ahead, the direct access to joint information between quantum objects enabled by quantum interference by-

passes the costly need to characterise each object individually and opens new possibilities for scalable quantum intelligent networks.

ACKNOWLEDGMENTS

The authors acknowledge Adam Taylor and Changhun Oh for useful discussions. R.B.P. thanks Bryn Bell for useful discussions regarding the PIC and acknowledges LioniX International for their service. MSK thanks Gyoyoung Jin for discussions on machine learning. This work was supported by UK Research and Innovation Future Leaders Fellowship (project: MR/W011794/1) and Guarantee Postdoctoral Fellowship (projects: EP/Y029127/1, EP/Y029631/1), Engineering and Physical Sciences Research Council (EPSRC) UK Quantum Technologies

Program’s hubs for Quantum Computing & Simulation (project: EP/T001062/1), Quantum Computing via Integrated and Interconnected Implementations (project: EP/Z53318X/1) and EPSRC projects (EP/W032643/1, EP/Y004752/1, and EP/W524323/1 [2928584]), EU Horizon 2020 Marie Skłodowska-Curie Innovation Training Network (project: 956071, ‘AppQInfo’), National Research Council of Canada (project QSP 062-2), and KIST through the Open Innovation fund and the National Research Foundation of Korea grant funded by the Korean government (MSIT) (No. RS-2024-00413957). Z.L. acknowledges partial funding support from ORCA Computing. H.Z. and L.Z. acknowledge funding support from National Natural Science Foundation of China (Grant Nos. 12347104, U24A2017), and the Natural Science Foundation of Jiangsu Province (Grant No. BK20243060).

-
- [1] C. M. Bishop, *Pattern Recognition and Machine Learning*, Information Science and Statistics (Springer, New York, NY, USA, 2006).
- [2] T. Hastie, R. Tibshirani, and J. Friedman, *The Elements of Statistical Learning*, Springer Series in Statistics (Springer, New York, NY, 2009).
- [3] A. Vaswani, N. Shazeer, N. Parmar, J. Uszkoreit, L. Jones, A. N. Gomez, L. Kaiser, and I. Polosukhin, Attention is all you need, in *Advances in Neural Information Processing Systems*, Vol. 30, edited by I. Guyon, U. V. Luxburg, S. Bengio, H. Wallach, R. Fergus, S. Vishwanathan, and R. Garnett (Curran Associates, Inc., 2017).
- [4] T. Brown, B. Mann, N. Ryder, M. Subbiah, J. D. Kaplan, P. Dhariwal, A. Neelakantan, P. Shyam, G. Sastry, A. Askell, S. Agarwal, A. Herbert-Voss, G. Krueger, T. Henighan, R. Child, A. Ramesh, D. Ziegler, J. Wu, C. Winter, C. Hesse, M. Chen, E. Sigler, M. Litwin, S. Gray, B. Chess, J. Clark, C. Berner, S. McCandlish, A. Radford, I. Sutskever, and D. Amodei, Language models are few-shot learners, in *Advances in Neural Information Processing Systems*, Vol. 33, edited by H. Larochelle, M. Ranzato, R. Hadsell, M. Balcan, and H. Lin (Curran Associates, Inc., 2020) pp. 1877–1901.
- [5] J. Biamonte, P. Wittek, N. Pancotti, P. Rebentrost, N. Wiebe, and S. Lloyd, Quantum machine learning, *Nature* **549**, 195 (2017).
- [6] V. Havlíček, A. D. Córcoles, K. Temme, A. W. Harrow, A. Kandala, J. M. Chow, and J. M. Gambetta, Supervised learning with quantum-enhanced feature spaces, *Nature* **567**, 209 (2019).
- [7] P. Rebentrost, M. Mohseni, and S. Lloyd, Quantum support vector machine for big data classification, *Physical Review Letters* **113**, 130503 (2014).
- [8] S. Jerbi, L. J. Fiderer, H. Poulsen Nautrup, J. M. Kübler, H. J. Briegel, and V. Dunjko, Quantum machine learning beyond kernel methods, *Nature Communications* **14**, 517 (2023).
- [9] M. Cerezo, A. Arrasmith, R. Babbush, S. C. Benjamin, S. Endo, K. Fujii, J. R. McClean, K. Mitarai, X. Yuan, L. Cincio, and P. J. Coles, Variational quantum algorithms, *Nature Reviews Physics* **3**, 625 (2021).
- [10] K. Beer, D. Bondarenko, T. Farrelly, T. J. Osborne, R. Salzmann, D. Scheiermann, and R. Wolf, Training deep quantum neural networks, *Nature Communications* **11**, 808 (2020).
- [11] S. Rethinasamy, R. Agarwal, K. Sharma, and M. M. Wilde, Estimating distinguishability measures on quantum computers, *Physical Review A* **108**, 012409 (2023).
- [12] Y. Liu, S. Arunachalam, and K. Temme, A rigorous and robust quantum speed-up in supervised machine learning, *Nature Physics* **17**, 1013 (2021).
- [13] H.-Y. Huang, M. Broughton, M. Mohseni, R. Babbush, S. Boixo, H. Neven, and J. R. McClean, Power of data in quantum machine learning, *Nature Communications* **12**, 2631 (2021).
- [14] E. Peters, J. Caldeira, A. Ho, S. Leichenauer, M. Mohseni, H. Neven, P. Spentzouris, D. Strain, and G. N. Perdue, Machine learning of high dimensional data on a noisy quantum processor, *npj Quantum Information* **7**, 161 (2021).
- [15] A. Abbas, D. Sutter, C. Zoufal, A. Lucchi, A. Figalli, and S. Woerner, The power of quantum neural networks, *Nature Computational Science* **1**, 403 (2021).
- [16] X. Pan, Z. Lu, W. Wang, Z. Hua, Y. Xu, W. Li, W. Cai, X. Li, H. Wang, Y.-P. Song, C.-L. Zou, D.-L. Deng, and L. Sun, Deep quantum neural networks on a superconducting processor, *Nature Communications* **14**, 4006 (2023).
- [17] Z. Yin, I. Agresti, G. de Felice, D. Brown, A. Toumi, C. Pentangelo, S. Piacentini, A. Crespi, F. Ceccarelli, R. Osellame, B. Coecke, and P. Walther, Experimental quantum-enhanced kernel-based machine learning on a photonic processor, *Nature Photonics* **19**, 1020 (2025).
- [18] F. Hoch, E. Caruccio, G. Rodari, T. Francalanci, A. Suprano, T. Giordani, G. Carvacho, N. Spagnolo, S. Koudia, M. Proietti, C. Liorni, F. Cerocchi, R. Albiero, N. Di Gianò, M. Gardina, F. Ceccarelli, G. Corrielli, U. Chabaud, R. Osellame, M. Dispenza, and F. Sciarrino, Quantum machine learning with adaptive boson

- sampling via post-selection, *Nature Communications* **16**, 902 (2025).
- [19] J. Haah, A. W. Harrow, Z. Ji, X. Wu, and N. Yu, Sample-optimal tomography of quantum states, in *Proceedings of the Forty-Eighth Annual ACM Symposium on Theory of Computing*, Stoc '16 (Association for Computing Machinery, New York, NY, USA, 2016) pp. 913–925.
- [20] A. Anshu, Z. Landau, and Y. Liu, Distributed Quantum inner product estimation, in *Proceedings of the 54th Annual ACM SIGACT Symposium on Theory of Computing*, Stoc 2022 (Association for Computing Machinery, New York, NY, USA, 2022) pp. 44–51.
- [21] H. Zhan, B. Wang, M. Mi, J. Xie, L. Xu, A. Zhang, and L. Zhang, Experimental benchmarking of quantum state overlap estimation strategies with photonic systems, *Light: Science & Applications* **14**, 83 (2025).
- [22] V. V. Shende, S. S. Bullock, and I. L. Markov, Synthesis of quantum logic circuits, in *Proceedings of the 2005 Asia and South Pacific Design Automation Conference*, ASP-DAC '05 (Association for Computing Machinery, New York, NY, USA, 2005) p. 272–275.
- [23] M. Cerezo, G. Verdon, H.-Y. Huang, L. Cincio, and P. J. Coles, Challenges and opportunities in quantum machine learning, *Nature Computational Science* **2**, 567 (2022).
- [24] H.-Y. Huang, M. Broughton, J. Cotler, S. Chen, J. Li, M. Mohseni, H. Neven, R. Babbush, R. Kueng, J. Preskill, and J. R. McClean, Quantum advantage in learning from experiments, *Science* **376**, 1182 (2022).
- [25] C. Oh, S. Chen, Y. Wong, S. Zhou, H.-Y. Huang, J. A. H. Nielsen, Z.-H. Liu, J. S. Neergaard-Nielsen, U. L. Andersen, L. Jiang, and J. Preskill, Entanglement-enabled advantage for learning a bosonic random displacement channel, *Physical Review Letters* **133**, 230604 (2024).
- [26] Z.-H. Liu, R. Brunel, E. E. B. Østergaard, O. Cordero, S. Chen, Y. Wong, J. A. H. Nielsen, A. B. Bregnsbo, S. Zhou, H.-Y. Huang, C. Oh, L. Jiang, J. Preskill, J. S. Neergaard-Nielsen, and U. L. Andersen, Quantum learning advantage on a scalable photonic platform, *Science* **389**, 1332 (2025).
- [27] E. Coroi and C. Oh, Exponential advantage in continuous-variable quantum state learning (2025), [arXiv:2501.17633 \[quant-ph\]](https://arxiv.org/abs/2501.17633).
- [28] M. S. Kim, J. Lee, and W. J. Munro, Experimentally realizable characterizations of continuous-variable Gaussian states, *Physical Review A* **66**, 030301 (2002).
- [29] J. C. Garcia-Escartin and P. Chamorro-Posada, SWAP test and Hong-Ou-Mandel effect are equivalent, *Physical Review A* **87**, 052330 (2013).
- [30] R. B. Patel, J. Ho, F. Ferreyrol, T. C. Ralph, and G. J. Pryde, A quantum Fredkin gate, *Science Advances* **2**, e1501531 (2016).
- [31] A. Zhang, H. Zhan, J. Liao, K. Zheng, T. Jiang, M. Mi, P. Yao, and L. Zhang, Quantum verification of NP problems with single photons and linear optics, *Light: Science & Applications* **10**, 169 (2021).
- [32] T. J. Volkoff and Y. Subaşı, Ancilla-free continuous-variable swap test, *Quantum* **6**, 800 (2022).
- [33] B. A. Bell and I. A. Walmsley, Further compactifying linear optical unitaries, *APL Photonics* **6**, 070804 (2021-07-01, 2021).
- [34] D. Gottesman, A. Kitaev, and J. Preskill, Encoding a qubit in an oscillator, *Physical Review A* **64**, 012310 (2001).
- [35] C. W. Helstrom, Quantum detection and estimation theory, *Journal of Statistical Physics* **1**, 231 (1969-06-01, 1969).
- [36] F. A. Mele, A. A. Mele, L. Bittel, J. Eisert, V. Giovannetti, L. Lami, L. Leone, and S. F. E. Oliviero, Learning quantum states of continuous-variable systems, *Nature Physics* **21**, 2002 (2025).
- [37] Y.-D. Wu, Y. Zhu, G. Chiribella, and N. Liu, Efficient learning of continuous-variable quantum states, *Physical Review Research* **6**, 033280 (2024).
- [38] A. Jacot, F. Gabriel, and C. Hongler, Neural tangent kernel: convergence and generalization in neural networks (Curran Associates Inc., Red Hook, NY, USA, 2018) p. 8580–8589.
- [39] S. Aaronson, X. Chen, E. Hazan, S. Kale, and A. Nayak, Online Learning of Quantum States, *Journal of Statistical Mechanics: Theory and Experiment* **2019**, 124019 (2019).
- [40] S. Lloyd and C. Weedbrook, Quantum generative adversarial learning, *Phys. Rev. Lett.* **121**, 040502 (2018).
- [41] J. C. Spall, An Overview of the Simultaneous Perturbation Method for Efficient Optimization, *JOHN HOPKINS APL TECHNICAL DIGEST* **19**, 482 (1998).
- [42] C. Ferrie, Self-guided quantum tomography, *Physical Review Letters* **113**, 190404 (2014).
- [43] M. Rambach, M. Qaryan, M. Kewming, C. Ferrie, A. G. White, and J. Romero, Robust and efficient high-dimensional quantum state tomography, *Physical Review Letters* **126**, 100402 (2021).
- [44] L. Serino, M. Rambach, B. Brecht, J. Romero, and C. Silberhorn, Self-guided tomography of time-frequency qudits, *Quantum Science and Technology* **10**, 025024 (2025).
- [45] J. Knörzner, X. Liu, B. F. Schiffer, and J. Tura, *Distributed quantum information processing: A review of recent progress* (2025), [arXiv:2510.15630 \[quant-ph\]](https://arxiv.org/abs/2510.15630).
- [46] J. F. Fitzsimons, Private quantum computation: An introduction to blind quantum computing and related protocols, *npj Quantum Information* **3**, 23 (2017).
- [47] S. Thanasilp, S. Wang, M. Cerezo, and Z. Holmes, Exponential concentration in quantum kernel methods, *Nature Communications* **15**, 5200 (2024).
- [48] M. Larocca, S. Thanasilp, S. Wang, K. Sharma, J. Biamonte, P. J. Coles, L. Cincio, J. R. McClean, Z. Holmes, and M. Cerezo, Barren plateaus in variational quantum computing, *Nature Reviews Physics* **7**, 174 (2025).
- [49] Y. Lim and C. Oh, *Classical algorithms for estimating expectation values in linear-optical circuits* (2025), [arXiv:2502.12882 \[quant-ph\]](https://arxiv.org/abs/2502.12882).
- [50] S. Konno, W. Asavanant, F. Hanamura, H. Nagayoshi, K. Fukui, A. Sakaguchi, R. Ide, F. China, M. Yabuno, S. Miki, H. Terai, K. Takase, M. Endo, P. Marek, R. Filip, P. van Loock, and A. Furusawa, Logical states for fault-tolerant quantum computation with propagating light, *Science* **383**, 289 (2024).
- [51] M. V. Larsen, J. E. Bourassa, S. Kocsis, J. F. Tasker, R. S. Chadwick, C. González-Arciniegas, J. Hastrup, C. E. Lopetegui-González, F. M. Miatto, A. Motamedi, *et al.*, Integrated photonic source of Gottesman–Kitaev–Preskill qubits, *Nature* **642**, 587 (2025).
- [52] S. Yu, J. Sun, K.-C. Chen, Z.-H. Yang, Z. Li, E. Mer, Y. K. Alwehaibi, S. H. Winston, D. M. D. Lopena, Z.-C. Zhang, G. Yang, R. Tao, M. Zhou, G. J. Machado, Y. Dong, R. Bondesan, V. Vedral, M. S. Kim, I. A. Walmsley, and R. B. Patel, *Extensible universal photonic*

- quantum computing with nonlinearity (2026), [arXiv:2602.06544 \[quant-ph\]](#).
- [53] A. E. Jones, A. J. Menssen, H. M. Chrzanowski, T. A. W. Wolterink, V. S. Shchesnovich, and I. A. Walmsley, Multiparticle Interference of Pairwise Distinguishable Photons, *Physical Review Letters* **125**, 123603 (2020).
- [54] J. Nöller, V. T. Tran, M. Gachechiladze, and R. Kueng, An infinite hierarchy of multi-copy quantum learning tasks (2025), [arXiv:2510.08070 \[quant-ph\]](#).
- [55] F. Y. Huo and N. F. Johnson, Capturing AI’s Attention: Physics of Repetition, Hallucination, Bias and Beyond (2025), [arXiv:2504.04600 \[cs\]](#).
- [56] J. Spall, Implementation of the simultaneous perturbation algorithm for stochastic optimization, *IEEE Transactions on Aerospace and Electronic Systems* **34**, 817 (1998).
- [57] S. M. Barnett and P. M. Radmore, *Methods in Theoretical Quantum Optics* (Oxford University Press, 2002).
- [58] A. Serafini, *Quantum Continuous Variables: A Primer of Theoretical Methods*, 2nd ed. (CRC press, Taylor & Francis Group, 2023).
- [59] W. P. Schleich, *Quantum Optics in Phase Space* (Wiley-VCH, Berlin, 2001).
- [60] W. Hoeffding, Probability inequalities for sums of bounded random variables, *Journal of the American Statistical Association* **58**, 13 (1963).
- [61] Q. Wang, Optimal trace distance and fidelity estimations for pure quantum states, *IEEE Transactions on Information Theory* **70**, 8791 (2024).
- [62] M. M. Wilde, *Quantum Information Theory* (Cambridge University Press, Cambridge, 2013).
- [63] C. G. H. Roeloffzen, M. Hoekman, E. J. Klein, L. S. Wevers, R. B. Timens, D. Marchenko, D. Geskus, R. Dekker, A. Alippi, R. Grootjans, A. Van Rees, R. M. Oldenbeuving, J. P. Epping, R. G. Heideman, K. Worhoff, A. Leinse, D. Geuzebroek, E. Schreuder, P. W. L. Van Dijk, I. Visscher, C. Taddei, Y. Fan, C. Taballione, Y. Liu, D. Marpaung, L. Zhuang, M. Benelajla, and K.-J. Boller, Low-Loss Si₃N₄ TriPleX Optical Waveguides: Technology and Applications Overview, *IEEE Journal of Selected Topics in Quantum Electronics* **24**, 1 (2018).
- [64] A. C. Hryciw, R. D. Kekatpure, S. Yerci, L. Dal Negro, and M. L. Brongersma, Thermo-optic tuning of erbium-doped amorphous silicon nitride microdisk resonators, *Applied Physics Letters* **98**, 041102 (2011).
- [65] A. Arbabi and L. L. Goddard, Measurements of the refractive indices and thermo-optic coefficients of Si₃N₄ and SiO₂ using microring resonances, *Optics Letters* **38**, 3878 (2013).
- [66] S. Bandyopadhyay, R. Hamerly, and D. Englund, Hardware error correction for programmable photonics, *Optica* **8**, 1247 (2021).
- [67] A. Fyrillas, O. Faure, N. Maring, J. Senellart, and N. Belabas, Scalable machine learning-assisted clear-box characterization for optimally controlled photonic circuits, *Optica* **11**, 427 (2024).
- [68] A. Youssry, Y. Yang, R. J. Chapman, B. Haylock, F. Lenzini, M. Lobino, and A. Peruzzo, Experimental graybox quantum system identification and control, *npj Quantum Information* **10**, 9 (2024).
- [69] C. Cortes and V. Vapnik, Support-vector networks, *Machine Learning* **20**, 273 (1995).
- [70] M. Andersen, J. Dahl, and L. Vandenberghe, CVXOPT – python software for convex optimization (2023).
- [71] F. Pedregosa, G. Varoquaux, A. Gramfort, V. Michel, B. Thirion, O. Grisel, M. Blondel, P. Prettenhofer, R. Weiss, V. Dubourg, J. Vanderplas, A. Passos, D. Cournapeau, M. Brucher, M. Perrot, and Édouard Duchesnay, Scikit-learn: Machine learning in python, *Journal of Machine Learning Research* **12**, 2825 (2011).

VIII. METHODS

A. Joint overlap estimation scheme

In our overlap estimation scheme, we interfere the two photonic states on balanced BSs before measuring one output register by PNRDs. The balanced BSs are described by unitary operator \hat{U}_{BS} that combine the modes pairwise:

$$\hat{U}_{\text{BS}}^\dagger \hat{a}_i^{(A)} \hat{U}_{\text{BS}} = \frac{1}{\sqrt{2}} \left(\hat{a}_i^{(A)} + \hat{a}_i^{(B)} \right), \quad (4)$$

$$\hat{U}_{\text{BS}}^\dagger \hat{a}_i^{(B)} \hat{U}_{\text{BS}} = \frac{1}{\sqrt{2}} \left(\hat{a}_i^{(A)} - \hat{a}_i^{(B)} \right). \quad (5)$$

Taking a partial trace over register (A) after the BS operation, the output state in register (B), denoted $\hat{\rho}^{(\text{out}, B)}$, has characteristic function,

$$\chi^{(\text{out}, B)}(\boldsymbol{\alpha}) = \chi^{(A)} \left(\frac{\boldsymbol{\alpha}}{\sqrt{2}} \right) \chi^{(B)} \left(-\frac{\boldsymbol{\alpha}}{\sqrt{2}} \right). \quad (6)$$

With a multiplicative rescaling, integrating Equation 6 over phase space recovers the overlap expression in Equation 1. This in fact equals the Wigner function of the output state at the origin of phase space, which can be measured by a total photon-number parity measurement across the M modes in register (B):

$$\begin{aligned} W^{(\text{out})}(\mathbf{0}) &= \frac{1}{\pi^{2M}} \int_{\mathcal{C}^M} d^{2M} \boldsymbol{\alpha} \chi^{(\text{out})}(\boldsymbol{\alpha}) \\ &= \text{Tr}_{(B)} \left[\hat{\rho}^{(\text{out}, B)} \hat{\Pi} \right] \end{aligned} \quad (7)$$

This recovers our overlap measurement scheme described by Equation 2.

Operationally, we can sample N shots and record $\{x_k\}_{k=1}^N$, where $x_k = +1$ for the k -th shot if the PNRDs measure an even total photon number and $x_k = -1$ if odd. From the binary outcomes, we build an unbiased estimator for the overlap value by $\tilde{Y} = \frac{1}{N} \sum_{k=1}^N x_k$, with expectation value $\langle \tilde{Y} \rangle = \text{Tr} [\hat{\rho}^{(A)} \hat{\rho}^{(B)}]$ by Equation 2.

B. Sample complexity optimality

The proof for Theorem 2 relies on converting the overlap estimation problem into a decisional quantum state discrimination problem, whose sample complexity can be bounded by applying Helstrom’s bound [20, 35].

In a quantum state discrimination problem, Alice chooses and prepares one state from $\hat{\sigma}_-^{\otimes N} = (\hat{\rho}_- \otimes$

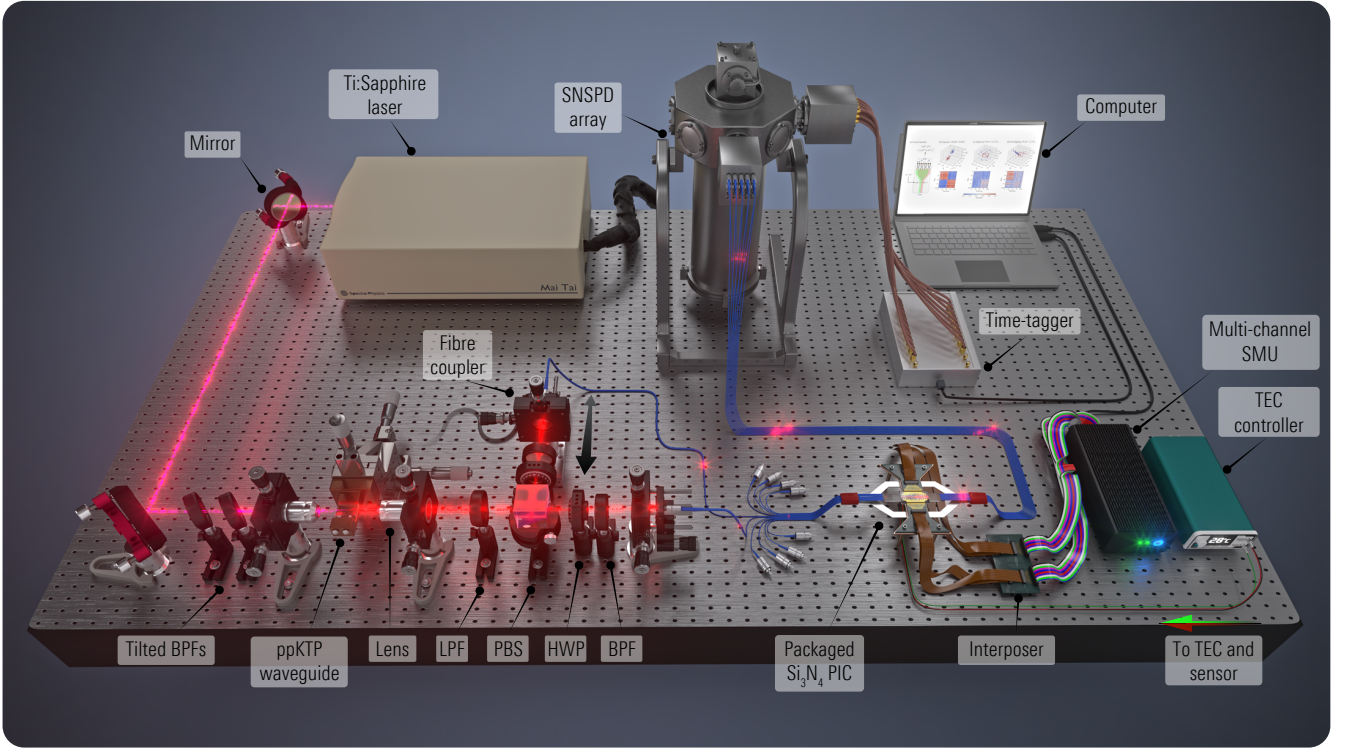


FIG. 5. An illustration of the experimental setup. A Ti:Sapphire laser produces 775 nm wavelength, ~ 1 ps long pulses, at 80 MHz, which are spectrally filtered to 0.9 nm bandwidth (full-width at half-maximum) using a pair of angle-tuned bandpass filters (BPF). The pulses are coupled into a 10 mm long ppKTP waveguide that is phase-matched for type-II SPDC. The residual pump is filtered using a long-pass filter (LPF) and a polarising beamsplitter (PBS) separates signal and idler pulses along separate paths, each containing a HWP and a BPF with a matched bandwidth to eliminate spectral correlations between signal and idler. The photon pair is delivered to the fully programmable Si_3N_4 PIC via polarisation-maintaining (PM) fibre. The thermo-optic phaseshifters on the PIC are programmed by a multi-channel source-measure unit (SMU), and a thermoelectric cooler (TEC) maintains the temperature of the PIC at 28°C . The eight output channels of the PIC are coupled to PM fibre, enabling detection by superconducting nanowire single-photon detectors (SNSPDs).

$|\phi_0\rangle\langle\phi_0|^{\otimes N}$ or $\hat{\sigma}_+^{\otimes N} = (\hat{\rho}_+ \otimes |\phi_0\rangle\langle\phi_0|)^{\otimes N}$ with equal prior probability, and sends it to Bob, where $\hat{\rho}_\pm = |\psi_\pm\rangle\langle\psi_\pm|$ are two pure states defined by,

$$|\psi_\pm\rangle = \sqrt{\frac{1}{2} \pm \epsilon} |\phi_0\rangle + \sqrt{\frac{1}{2} \mp \epsilon} |\phi_1\rangle. \quad (8)$$

The pure states $|\phi_{0/1}\rangle$ need to be orthogonal—they can be the computational basis states in DV systems or squeezed vacuum and single-photon-subtracted squeezed vacuum states in CV systems.

For the quantum state discrimination problem, Bob can distinguish between $\hat{\sigma}_\pm^{\otimes N}$ with success probability $P_{\text{success}} \geq 1 - \delta$ if N suffices to estimate $\text{Tr}[\hat{\rho}_- \otimes |\phi_0\rangle\langle\phi_0|]$ to within ϵ error with $1 - \delta$ probability. However, by Helstrom's bound, the success probability is also upper-bounded by the trace distance between $\hat{\sigma}_\pm^{\otimes N}$,

$$P_{\text{success}} \leq \frac{1}{2} \left(1 + \frac{1}{2} \|\hat{\sigma}_-^{\otimes N} - \hat{\sigma}_+^{\otimes N}\|_1 \right) \leq \frac{1}{2} + \epsilon\sqrt{N}, \quad (9)$$

thus giving the lower bound $N = \Omega(\epsilon^{-2}(1 - 2\delta)^2/4)$ in Theorem 2, which simplifies to $N = \Omega(\epsilon^{-2})$ if we for

example set $\delta = \frac{1}{3}$. For any method that solves the overlap estimation problem, the special states we defined above, $\hat{\sigma}_\pm^{\otimes N}$, constitute worst-case instances where no method can guarantee a sample complexity better than $N = O(\epsilon^{-2})$ without violating the Helstrom's bound. The formal proof of Theorem 2 is provided in the Supplementary Information.

C. Distributed overlap estimation for CV states

In the main text, we consider a specific distributed overlap estimation method for self-reflective CV states. For these states, independent characterisation is efficient, whereas distributed overlap estimation remains inefficient.

A state is self-reflective if there exists a set of axes in phase space through the origin, about which the reflection of the state is itself. The worst-case complexity of estimating the characteristic function of CV states is exponential in the mode number [27]. However, for self-reflective states, an efficient N -copy measurement exists

that can estimate their $\chi(\boldsymbol{\alpha}_i)$ up to additive error $\tilde{\epsilon}$ for L points in phase space given only logarithmic sample complexity $N = O(\tilde{\epsilon}^{-4} \log(L))$ [37].

This provides a route to distributed overlap estimation. Alice and Bob respectively produce characteristic function estimators, $\tilde{\chi}^{(A/B)}(\boldsymbol{\alpha}_i)$, with error $\tilde{\epsilon}$ for L points in some sub-space \mathcal{A} . Then they estimate the overlap by Monte-Carlo approximation to Equation 1: $\tilde{Y} = \frac{|\mathcal{A}|}{\pi^M L} \sum_{i=1}^L \tilde{\chi}^{(A)}(\boldsymbol{\alpha}_i) \tilde{\chi}^{(B)}(-\boldsymbol{\alpha}_i)$. If we bound the energy of the CV state and assume the integral of Equation 1 is negligible outside \mathcal{A} , then \tilde{Y} estimates the overlap with error ϵ , if $\tilde{\epsilon} = \frac{\pi^M}{8|\mathcal{A}|} \epsilon$ and $L = \left(\frac{4\sigma_L |\mathcal{A}|}{\pi^M \epsilon}\right)^2$, where M is the mode number. The Monte-Carlo error is given by $(\sigma_L)^2 = \sum_{i=1}^L \left(f(\boldsymbol{\alpha}_i) - \sum_{j=1}^L f(\boldsymbol{\alpha}_j)/L\right)^2 / (L-1)$ for $f(\boldsymbol{\alpha}_i) = \chi^{(A)}(\boldsymbol{\alpha}_i) \chi^{(B)}(-\boldsymbol{\alpha}_i)$ and can be estimated using the $\tilde{\chi}^{(A/B)}$ estimators. The resulting sample complexity is $N = O(|\mathcal{A}|^4 / \epsilon^4 \pi^{4M} \log(|\mathcal{A}|^2 \sigma_L^2 / \epsilon^2 \pi^{2M}))$.

However, if we adopt a commonly used mode-extensive energy constraint on the CV state [27, 36], such that the sub-space \mathcal{A} is a $2M$ -dimensional hypersphere with radius $|\boldsymbol{\alpha}| = \sqrt{\kappa M}$, then it has volume, $|\mathcal{A}| = \frac{(\pi \kappa M)^M}{M!} = O\left(\frac{(\epsilon \pi \kappa)^M}{\sqrt{2\pi M}}\right)$. As a result, the overall sample complexity is still exponential in M , as stated informally in Theorem 3 (formal proof in Supplementary Information).

D. Photon source

Photon pairs are generated using a type-II SPDC source based on a ppKTP waveguide (AdvR) pumped by a mode-locked Ti:Sapphire laser (Spectra-Physics Mai Tai, 80 MHz repetition rate, 775 nm), with the pump spectrum filtered to a 0.9 nm FWHM using a pair of 3 nm bandpass filters (Thorlabs FBH780-3). The source produces collinear, orthogonally polarised signal and idler photons at 1550 nm, which are separated by a polarising beam splitter and mildly filtered using a 10 nm bandpass filter, before being coupled into polarisation-maintaining (PM) fibres, and injected into a chip-based photonic circuit with output modes detected by SNSPDs. At a pump power 65 μ W, the detected signal-idler coincidence rate is 5.5 kHz, while higher-order photon-number contributions are suppressed to below 50 per second. Two-photon indistinguishability is characterised via on-chip Hong-Ou-Mandel interference with a variable delay in the signal mode, yielding a visibility of 95.4%.

E. Photonic chip calibration

The silicon nitride chip used in this work, fabricated by LioniX, comprises a 10×10 array of thermo-optically tunable phaseshifters and is packaged with PM fibre arrays for both input and output coupling (PHIX Photonics Assembly BV). The chip implements a 10-mode

universal linear-optical interferometer. Before performing QML tasks, each phaseshifter is carefully calibrated, with directional coupler imperfections and thermal crosstalk taken into account. We further develop a crosstalk-mitigation method that improves the average fidelity of the output coincidence distribution to 0.980 ± 0.006 . In addition, a digital simulator of the chip is designed to quantify the detrimental effects of thermal crosstalk and to validate the effectiveness of our calibration. Further details of the calibration methods and the simulator are provided in the Supplementary Information.

F. Support vector machine

Not all datasets are linearly separable in their original space. In this scenario, the trick is to find a non-linear kernel function that maps the data into a high-dimensional space where the task can be reduced to linear classification. For data vectors with dimension d , denoted $\boldsymbol{x}^{(i)} \in \mathbb{R}^d$, one can encode the data into some quantum state $|\psi(\boldsymbol{x}^{(i)})\rangle$, which constitutes a quantum feature map into Hilbert space \mathcal{H} .

For each dataset classified by SVM in main text, we generate a training subset of 100 binary-labelled data instances, $\{|\psi(\boldsymbol{x}^{(i)})\rangle, y^{(i)}\}_{i=1}^{100}$. By evaluating the overlap between each pair of data instances, we construct a 100×100 overlap matrix, \mathbf{K} , whose elements are given by $K_{ij} = |\langle \psi(\boldsymbol{x}^{(i)}) | \psi(\boldsymbol{x}^{(j)}) \rangle|^2$. We aim to find a vectorised classifier weight, $\boldsymbol{\beta} = (\beta^{(1)}, \dots, \beta^{(m)})^T$, which maximises the hyperplane separation between the two different classes. We do so by solving the following constrained optimisation problem:

$$\begin{aligned} \min_{\boldsymbol{\beta}} \quad & \frac{1}{2} \boldsymbol{\beta}^T (\mathbf{y}^T \mathbf{K} \mathbf{y}) \boldsymbol{\beta} - \sum_i \beta_i, \\ \text{subject to} \quad & 0 \leq \beta^{(i)} \leq C, \\ & \mathbf{y}^T \boldsymbol{\beta} = 0, \end{aligned} \quad (10)$$

where vector $\mathbf{y} = (y^{(1)}, \dots, y^{(m)})^T$ is the vectorised training labels, and C is a slack constant for soft-margin optimisation, which we set to $C = 0.8$. Then we define a bias correction term, b , by

$$b = \frac{1}{100} \sum_{j=1}^{100} \left(y^{(j)} - \sum_{i=1}^{100} \beta^{(i)} y^{(j)} K_{ji} \right). \quad (11)$$

As a result, for any new unseen data, \boldsymbol{x} , encoded in qudit $|\psi(\boldsymbol{x})\rangle$, we compute its overlap with each training qudit and predict its label by,

$$\hat{y}(\boldsymbol{x}) = \text{sign} \left(\sum_{i=1}^{100} \beta^{(i)} y^{(i)} \left| \langle \psi(\boldsymbol{x}^{(i)}) | \psi(\boldsymbol{x}) \rangle \right|^2 + b \right). \quad (12)$$

In practice, however, the classifier weight $\beta^{(i)}$ is typically non-zero for a subset of the training data, which is re-

ferred to as the ‘support vectors’ and to which we can limit our overlap evaluations.

For the three datasets shown in Fig. 3 (linearly separable, concentric spheres and overlapping blobs), we generate 200 phase vectors according to the dataset structure, which are randomly divided into training and test subsets. The amplitudes of the qudit, A_j in Equation 3, are chosen to optimise the classification accuracy across the three datasets in numerical simulations. Details of the SVM implementation are provided in the Supplementary Information.

G. Simultaneous perturbation stochastic approximation

For online learning of quantum data, we implement the SPSA algorithm proposed and detailed in Ref. [41, 56]. The routine works by randomly perturbing the reference state at each iteration, and use the overlap evaluation at both directions of the perturbation for gradient estimation. Then the state is updated along the descent direction, before being perturbed at the next iteration.

In SPSA, we seek to minimise a cost function, which in this implementation is defined as one minus the overlap between the target and reference qudit states:

$$c(\boldsymbol{\theta}) = 1 - \left| \langle \psi(\mathbf{x}^{(t)}) | \psi(\boldsymbol{\theta}) \rangle \right|^2. \quad (13)$$

In the k -th iteration, where the reference qudit has phase, $\boldsymbol{\theta}^{(k)}$, we evaluate the cost function at $c(\boldsymbol{\theta}^{(k)} \pm \boldsymbol{\Delta}^{(k)} t^{(k)})$, where $\boldsymbol{\Delta}^{(k)} \in \{\pm 1\}^{\otimes 3}$ is a random perturbation vector. This allows us to approximate the local gradient (vectorised) to be,

$$\mathbf{g}(\boldsymbol{\theta}^{(k)}) = \frac{c(\boldsymbol{\theta}^{(k)} + \boldsymbol{\Delta}^{(k)} t^{(k)}) - c(\boldsymbol{\theta}^{(k)} - \boldsymbol{\Delta}^{(k)} t^{(k)})}{2t^{(k)} \boldsymbol{\Delta}^{(k)}}. \quad (14)$$

Then, we update the phase vector for the $(k+1)$ -th iteration to be, $\boldsymbol{\theta}^{(k+1)} = \boldsymbol{\theta}^{(k)} - a^{(k)} \mathbf{g}(\boldsymbol{\theta}^{(k)})$.

The gain coefficient and perturbation coefficient decay with the number of iterations as:

$$a^{(k)} = \frac{a}{(A + k + 1)^\alpha}, \quad (15)$$

$$t^{(k)} = \frac{t}{(k + 1)^\gamma}. \quad (16)$$

For constants, we choose $\alpha = 0.602$, $\gamma = 0.101$, $A = 10$, $a = 1.6$ for 500 iterations per optimisation. At the start of each optimisation, we evaluate the initial cost function at the 0-th iteration five times and set coefficient t to be twice the standard deviation of the function value.

We repeat the optimisation for ten target states with randomly selected phases, and for different number of state copies per overlap evaluation, as explained in the main text. The results are summarised in Fig. 4 with further details provided in the Supplementary Information.

H. Data collection

The overlap estimation in our experiment consists of measuring eight optical modes with SNSPDs (Photon Spot), which are non-photon-number-resolving detectors but suffice for measuring the overlap between two single-photon qudit states. The two output registers, A/B , labelled in Equation 2, correspond to the odd-number-labelled modes $\{1, 3, 5, 7\}$ and even-number-labelled modes $\{2, 4, 6, 8\}$, respectively. Consequently, an odd-parity total-photon-number measurement corresponds to a coincidence detection between two modes k and l where $k + l$ is an odd number.

In measurement, we post-select outputs on two-photon coincidence events. Due to the suppression of higher-order photon-number components in the photon source, post-selection eliminates the effect of photon loss without introducing unwanted terms to the computation. For a total of N two-photon detection events, comprising N_{odd} odd-parity events, the overlap estimator is constructed by,

$$\tilde{Y} = 1 - 2(1 - R) \frac{N_{\text{odd}}}{N}, \quad (17)$$

where $R = \sum_{i=0}^3 A_i^4 < 1$. Here, A_i is the encoded amplitude of the qudit states (Equation 3) and are experimentally validated. We treat these amplitudes as known quantities, as data is encoded exclusively in the phase-degrees of freedom. Physically, the term R represents the bunching probability, which is the probability of two photons arriving in the same output mode. These instances contribute to even-parity events but are discarded by our post-selection process. This term can be removed in an improved future implementation with intrinsic PNRDs. Additionally, Equation 17 can be rescaled by the Hong-Ou-Mandel interference visibility, though this rescaling was found to have negligible impact on the final accuracy of the QML tasks demonstrated in this work.

For the quantum data classification experiment, we limit each overlap estimation to $N = 1000$ detected coincidences. During data collection, we continuously monitor the coincidence rate and adjust the collection window to measure 15000 coincidence events per measurement. In post-processing, we randomly sample 1000 events to perform the overlap estimation, and bootstrap the process 1000 times. This provides an error estimate for each overlap value, which is then propagated using Monte-Carlo simulations to estimate the error of the final classification accuracy (shown in Fig. 3).

In the quantum data online learning experiment, the adaptive nature of the measurement process precludes the use of downsampling and bootstrapping. Instead, we lower the coincidence rate such that each collection window directly produces the target total coincidence number per overlap evaluation. This collection window is continuously monitored and adjusted to accommodate count-rate fluctuations in the photon source. The

experiment was repeated for total coincidence numbers $N = 10^2, 10^3$ and 10^4 , as presented in Fig. 4.

Supplementary Information: Machine learning of quantum data using optimal similarity measurements

SI. PHOTONIC STATES

A. Preliminary

In this section, we give an overview of bosonic systems and derive some useful identities. More details can be found in Refs. [57–59].

In the rest of the document, without further explanation, we consider M -mode bosonic states described by their density operators $\hat{\rho}$. For discrete-variable (DV) states, the density operator $\hat{\rho}$ acts on a d -dimensional Hilbert space. For continuous-variable (CV) states, the Hilbert space dimension is theoretically infinite.

An M -mode bosonic system is defined by its bosonic annihilation and creation operators. For the k -th mode, the creation and annihilation operators are denoted as $\hat{a}_k^\dagger, \hat{a}_k$ respectively, with commutation relations given by

$$[\hat{a}_k, \hat{a}_{k'}^\dagger] = \delta_{k,k'}, \quad [\hat{a}_k, \hat{a}_{k'}] = [\hat{a}_k^\dagger, \hat{a}_{k'}^\dagger] = 0. \quad (\text{S1})$$

The photon number operator of the k -th mode is denoted,

$$\hat{n}_k := \hat{a}_k^\dagger \hat{a}_k. \quad (\text{S2})$$

And we also define a total photon number parity operator:

$$\hat{\Pi} := (-1)^{\sum_{k=1}^M \hat{n}_k}. \quad (\text{S3})$$

The M -mode displacement operator is defined as

$$\hat{D}(\boldsymbol{\alpha}) := e^{\sum_{k=1}^M (\alpha_k \hat{a}_k^\dagger - \alpha_k^* \hat{a}_k)} \quad (\text{S4})$$

for a complex displacement vector, $\boldsymbol{\alpha} = (\alpha_1, \dots, \alpha_M) \in \mathbb{C}^M$, by which the state is displaced in phase space. Acting the displacement operator onto the vacuum state generates an M -mode coherent state, $|\boldsymbol{\alpha}\rangle = \hat{D}(\boldsymbol{\alpha})|0\rangle$. Coherent states are not orthogonal but form an overcomplete basis of the Hilbert space, allowing the identity operator to be decomposed as

$$\hat{I} = \frac{1}{\pi^M} \int_{\mathbb{C}^M} d^{2M} \boldsymbol{\alpha} |\boldsymbol{\alpha}\rangle \langle \boldsymbol{\alpha}|, \quad (\text{S5})$$

where the integral over the multi-mode phase space is $\frac{1}{\pi^M} \int_{\mathbb{C}^M} d^{2M} \boldsymbol{\alpha} = \left(\frac{1}{\pi} \int_{\mathbb{C}} d^2 \alpha_1\right) \dots \left(\frac{1}{\pi} \int_{\mathbb{C}} d^2 \alpha_M\right)$.

The trace of any trace class operator, \hat{O} can be expressed as an integral over the coherent state basis:

$$\text{Tr}[\hat{O}] = \frac{1}{\pi^M} \int_{\mathbb{C}^M} d^{2M} \boldsymbol{\alpha} \langle \boldsymbol{\alpha} | \hat{O} | \boldsymbol{\alpha} \rangle. \quad (\text{S6})$$

The integral of the displacement operator over phase space is [57],

$$\begin{aligned} \frac{1}{(2\pi)^M} \int_{\mathbb{C}^M} d^{2M} \boldsymbol{\alpha} \hat{D}(\boldsymbol{\alpha}) &= \prod_{k=1}^M \left(\frac{1}{2\pi} \int_{\mathbb{C}} d^2 \alpha_k \hat{D}_k(\alpha_k) \right) \\ &= \prod_{k=1}^M \left(\sum_{m=0}^{\infty} \frac{(-2)^m}{m!} (\hat{a}_k^\dagger)^m \hat{a}_k^m \right) \\ &= \prod_{k=1}^M \left((-1)^{\hat{a}_k^\dagger \hat{a}_k} \right) = (-1)^{\sum_{k=1}^M \hat{n}_k} \equiv \hat{\Pi} \end{aligned} \quad (\text{S7})$$

which is the total photon number parity operator in Equation S3.

Using Equation S6, the trace of the displacement operator is

$$\begin{aligned} \text{Tr} [\hat{D}(\boldsymbol{\alpha})] &= \frac{1}{\pi^M} \int_{\mathbb{C}^M} d^{2M} \boldsymbol{\beta} \langle \boldsymbol{\beta} | \hat{D}(\boldsymbol{\alpha}) | \boldsymbol{\beta} \rangle \\ &= \frac{1}{\pi^M} \int_{\mathbb{C}^M} d^{2M} \boldsymbol{\beta} e^{\boldsymbol{\beta}^\dagger \boldsymbol{\alpha} - \boldsymbol{\alpha}^\dagger \boldsymbol{\beta}} e^{-\frac{1}{2} \boldsymbol{\alpha}^\dagger \boldsymbol{\alpha}} = \pi^M \delta^{(2M)}(\boldsymbol{\alpha}). \end{aligned} \quad (\text{S8})$$

B. Description of photonic states

Leveraging the completeness relation of the coherent states, any M -mode state with density operator $\hat{\rho}$ can be decomposed as,

$$\hat{\rho} = \frac{1}{\pi^M} \int_{\mathbb{C}^M} d^{2M} \boldsymbol{\alpha} \chi(\boldsymbol{\alpha}) \hat{D}(-\boldsymbol{\alpha}), \quad (\text{S9})$$

for characteristic function

$$\chi(\boldsymbol{\alpha}) := \text{Tr} \left[\hat{D}(\boldsymbol{\alpha}) \hat{\rho} \right]. \quad (\text{S10})$$

A photonic state can be fully described by its characteristic function.

Alternatively, we can take the complex Fourier transform of Equation S10 and derive the Wigner function description of the state, which is

$$W(\boldsymbol{\alpha}) = \frac{1}{\pi^{2M}} \int_{\mathbb{C}^M} d^{2M} \boldsymbol{\beta} e^{\boldsymbol{\beta}^\dagger \boldsymbol{\alpha} - \boldsymbol{\alpha}^\dagger \boldsymbol{\beta}} \chi(\boldsymbol{\beta}). \quad (\text{S11})$$

Specifically, we have,

$$\begin{aligned} e^{\boldsymbol{\beta}^\dagger \boldsymbol{\alpha} - \boldsymbol{\alpha}^\dagger \boldsymbol{\beta}} \hat{D}(\boldsymbol{\beta}) &= e^{\sum_{k=1}^M [\beta_k (\hat{a}_k^\dagger - \alpha_k^*) - \beta_k^* (\hat{a}_k - \alpha_k)]} \\ &= e^{\sum_{k=1}^M \hat{D}_k^\dagger(-\alpha_k) (\beta_k \hat{a}_k^\dagger - \beta_k^* \hat{a}_k) \hat{D}_k(-\alpha_k)} \\ &= \hat{D}^\dagger(-\boldsymbol{\alpha}) \hat{D}(\boldsymbol{\beta}) \hat{D}(-\boldsymbol{\alpha}), \end{aligned} \quad (\text{S12})$$

which, after substituting into Equation S11 and using the definition of Equation S10, allows us to write the Wigner function explicitly as,

$$\begin{aligned} W(\boldsymbol{\alpha}) &= \frac{1}{\pi^{2M}} \int_{\mathbb{C}^M} d^{2M} \boldsymbol{\beta} \text{Tr} \left[e^{\boldsymbol{\beta}^\dagger \boldsymbol{\alpha} - \boldsymbol{\alpha}^\dagger \boldsymbol{\beta}} \hat{D}(\boldsymbol{\beta}) \hat{\rho} \right] \\ &= \left(\frac{2}{\pi} \right)^M \text{Tr} \left[\hat{D}(\boldsymbol{\alpha}) \hat{\rho} \hat{D}^\dagger(\boldsymbol{\alpha}) \frac{1}{(2\pi)^M} \int_{\mathbb{C}^M} d^{2M} \boldsymbol{\beta} \hat{D}(\boldsymbol{\beta}) \right] \\ &= \left(\frac{2}{\pi} \right)^M \text{Tr} \left[\hat{D}(\boldsymbol{\alpha}) \hat{\rho} \hat{D}^\dagger(\boldsymbol{\alpha}) \hat{\Pi} \right], \end{aligned} \quad (\text{S13})$$

where we used Equation S7 to evaluate the integral of the displacement operator. Operationally, this allows us to directly measure the Wigner function of a quantum state by first displacing it in phase space, and then measuring its total photon number parity. In particular, at origin of phase space, the displacement is zero and we can directly measure the Wigner function by PNRDs without displacement:

$$W(\mathbf{0}) = \left(\frac{2}{\pi} \right)^M \text{Tr} \left[\hat{\rho} \hat{\Pi} \right]. \quad (\text{S14})$$

C. Overlap between two states

For two M -mode states, $\hat{\rho}^{(A)}$ and $\hat{\rho}^{(B)}$, their overlap can be defined as $\text{Tr} [\hat{\rho}^{(A)} \hat{\rho}^{(B)}]$. For two pure states, $\hat{\rho}^{(A)} = |\psi\rangle\langle\psi|$, $\hat{\rho}^{(B)} = |\phi\rangle\langle\phi|$, this definition equals $|\langle\psi|\phi\rangle|^2$. Expressed in terms of their characteristic functions, $\chi^{(A)}(\boldsymbol{\alpha})$, $\chi^{(B)}(\boldsymbol{\alpha})$, this is

$$\begin{aligned} \text{Tr} \left[\hat{\rho}^{(A)} \hat{\rho}^{(B)} \right] &= \frac{1}{\pi^{2M}} \int_{\mathbb{C}^M} d^{2M} \boldsymbol{\alpha} \int_{\mathbb{C}^M} d^{2M} \boldsymbol{\beta} \chi^{(A)}(\boldsymbol{\alpha}) \chi^{(B)}(\boldsymbol{\beta}) \text{Tr} \left[\hat{D}(-\boldsymbol{\alpha}) \hat{D}(-\boldsymbol{\beta}) \right] \\ &= \frac{1}{\pi^{2M}} \int_{\mathbb{C}^{2M}} d^{2M} \boldsymbol{\alpha} d^{2M} \boldsymbol{\beta} \chi^{(A)}(\boldsymbol{\alpha}) \chi^{(B)}(\boldsymbol{\beta}) \text{Tr} \left[\hat{D}(-\boldsymbol{\alpha} - \boldsymbol{\beta}) \right] e^{\frac{1}{2}(\boldsymbol{\beta}^\dagger \boldsymbol{\alpha} - \boldsymbol{\alpha}^\dagger \boldsymbol{\beta})} \\ &= \frac{1}{\pi^M} \int_{\mathbb{C}^{2M}} d^{2M} \boldsymbol{\alpha} \chi^{(A)}(\boldsymbol{\alpha}) \chi^{(B)}(-\boldsymbol{\alpha}), \end{aligned} \quad (\text{S15})$$

where in the second line we used the combination of two displacement operators, $\hat{D}(\boldsymbol{\alpha}) \hat{D}(\boldsymbol{\beta}) = e^{\frac{1}{2}(\boldsymbol{\beta}^\dagger \boldsymbol{\alpha} - \boldsymbol{\alpha}^\dagger \boldsymbol{\beta})} \hat{D}(\boldsymbol{\alpha} + \boldsymbol{\beta})$.

SII. JOINT OVERLAP ESTIMATION

In this section, we explicitly derive the joint overlap estimation scheme given in the main text, including its sample complexity and the optimality of the sample complexity.

A. Derivation

We consider two M -mode states, $\hat{\rho}^{(A)}$ and $\hat{\rho}^{(B)}$, described by characteristic functions $\chi^{(A/B)}(\boldsymbol{\alpha})$. Each state occupies half of a total $2M$ -mode system. If we divide the $2M$ modes into two registers, we will use superscripts (A/B) to label the register where the input state originally sits in, and subscripts $i = 1, \dots, M$ to label the modes within each register.

We interfere the two M -mode states pairwise on balanced beamsplitters (BSs) described by unitary operator, \hat{B} , with action

$$\hat{B}^\dagger \hat{a}_i^{(A)} \hat{B} = \frac{1}{\sqrt{2}} \left(\hat{a}_i^{(A)} + \hat{a}_i^{(B)} \right), \quad \hat{B}^\dagger \hat{a}_i^{(B)} \hat{B} = \frac{1}{\sqrt{2}} \left(\hat{a}_i^{(A)} - \hat{a}_i^{(B)} \right). \quad (\text{S16})$$

For example, a $2M$ -mode displacement described by $\hat{D}^{(A)}(\boldsymbol{\alpha}) \otimes \hat{D}^{(B)}(\boldsymbol{\beta})$ for complex vectors $\boldsymbol{\alpha}, \boldsymbol{\beta} \in \mathbb{C}^M$ undergoes the following transformation under the beamsplitters:

$$\hat{B}^\dagger \left(\hat{D}^{(A)}(\boldsymbol{\alpha}) \otimes \hat{D}^{(B)}(\boldsymbol{\beta}) \right) \hat{B} = \hat{D}^{(A)} \left(\frac{\boldsymbol{\alpha} + \boldsymbol{\beta}}{\sqrt{2}} \right) \otimes \hat{D}^{(B)} \left(\frac{\boldsymbol{\alpha} - \boldsymbol{\beta}}{\sqrt{2}} \right). \quad (\text{S17})$$

Expanding the states, $\hat{\rho}^{(A/B)}$, in terms of Equation S9 and using Equation S17, we derive,

$$\hat{B}^\dagger \left(\hat{\rho}^{(A)} \otimes \hat{\rho}^{(B)} \right) \hat{B} = \frac{1}{\pi^{2M}} \int_{\mathbb{C}^M} d^{2M} \boldsymbol{\alpha} \int_{\mathbb{C}^M} d^{2M} \boldsymbol{\beta} \chi^{(A)}(\boldsymbol{\alpha}) \chi^{(B)}(\boldsymbol{\beta}) \hat{D}^{(A)} \left(-\frac{\boldsymbol{\alpha} + \boldsymbol{\beta}}{\sqrt{2}} \right) \hat{D}^{(B)} \left(-\frac{\boldsymbol{\alpha} - \boldsymbol{\beta}}{\sqrt{2}} \right). \quad (\text{S18})$$

Taking a partial trace over the register (A) , and using Equation S8, the output state in the register (B) is

$$\hat{\rho}^{(\text{out})} = \text{Tr}_{(A)} \left[\hat{B}^\dagger \left(\hat{\rho}^{(A)} \otimes \hat{\rho}^{(B)} \right) \hat{B} \right] = \frac{1}{\pi^M} \int_{\mathbb{C}^M} d^{2M} \boldsymbol{\gamma} \chi^{(A)} \left(\frac{\boldsymbol{\gamma}}{\sqrt{2}} \right) \chi^{(B)} \left(-\frac{\boldsymbol{\gamma}}{\sqrt{2}} \right) \hat{D}^{(B)}(-\boldsymbol{\gamma}), \quad (\text{S19})$$

which means it has characteristic function $\chi^{(\text{out})}(\boldsymbol{\gamma}) = \chi^{(A)} \left(\frac{\boldsymbol{\gamma}}{\sqrt{2}} \right) \chi^{(B)} \left(-\frac{\boldsymbol{\gamma}}{\sqrt{2}} \right)$.

Using Equation S11, the Wigner function of the output state at origin of phase space is given by

$$\begin{aligned} W^{(\text{out})}(\mathbf{0}) &= \frac{1}{\pi^{2M}} \int_{\mathbb{C}^M} d^{2M} \boldsymbol{\gamma} \chi^{(\text{out})}(\boldsymbol{\gamma}) \\ &= \frac{2^M}{\pi^{2M}} \int_{\mathbb{C}^M} d^{2M} \boldsymbol{\alpha} \chi^{(A)}(\boldsymbol{\alpha}) \chi^{(B)}(-\boldsymbol{\alpha}) \\ &= \left(\frac{2}{\pi} \right)^M \text{Tr} \left[\hat{\rho}^{(A)} \hat{\rho}^{(B)} \right]. \end{aligned} \quad (\text{S20})$$

In the second line, we made a substitution of integration variable, $\boldsymbol{\gamma} = \sqrt{2}\boldsymbol{\alpha}$, and in the third line we used the definition of overlap in Equation S15.

Finally, we can equate Equation S20 to Equation S14. This gives,

$$\text{Tr} \left[\hat{\rho}^{(A)} \hat{\rho}^{(B)} \right] = \text{Tr}_{(B)} \left[\text{Tr}_{(A)} \left[\hat{B}^\dagger \left(\hat{\rho}^{(A)} \otimes \hat{\rho}^{(B)} \right) \hat{B} \right] \hat{\Pi} \right]. \quad (\text{S21})$$

Operationally, Equation S21 means we can estimate the overlap between two photonic states by first interfering them on balanced BSs before measuring half of the output register on PNRDs for their photon-number parity.

B. Sample complexity

The parity measurement in Equation S21 is a binary outcome measurement. Since the sample variance is a fixed quantity for this type of measurements, derivation of their sample complexity commonly uses the Hoeffding's

inequality: Let x_1, \dots, x_N be independent random variables such that $a_k \leq x_k \leq b_k$ for all $k \in [1, N]$. For the sum of these random variables, $S_N = \sum_{k=1}^N x_k$, Hoeffding's inequality states that for all $t > 0$, we have [60]

$$\Pr(|S_N - \langle S_N \rangle| \geq t) \leq 2 \exp\left(-\frac{2t^2}{\sum_{k=1}^N (b_k - a_k)^2}\right), \quad (\text{S22})$$

where $\langle S_N \rangle$ is the expectation value of S_N .

The sample complexity of our joint overlap estimation scheme is stated in Theorem 1 of the main text, which we restate below and give a full proof.

Theorem S1. (Theorem 1 in main text.) *Given N copies of $\hat{\rho}^{(A)} \otimes \hat{\rho}^{(B)}$ and some constants $\epsilon, \delta \in (0, \frac{1}{2})$, by use of balanced BSs and PNRDs, the overlap $\text{Tr}[\hat{\rho}^{(A)} \hat{\rho}^{(B)}]$ can be estimated to within additive error ϵ with success probability at least $1 - \delta$ for sample complexity $N = 2\epsilon^{-2} \log(2\delta^{-1})$.*

Proof. The overlap can be estimated by the parity measurement in Equation S21, which uses only balanced BSs and PNRDs. Suppose we perform the experiment for N shots, and the result of each shot is recorded as x_k for $k \in [1, N]$, where $x_k = 1$ if an even photon number is measured and $x_k = -1$ if odd. They satisfy $-1 \leq x_k \leq 1$, such that $a_k = -1, b_k = 1$ for $k \in [1, N]$ in Equation S22. Then the estimator, $\tilde{Y} = \frac{1}{N} \sum_{k=1}^N x_k$, is an unbiased estimator for the overlap, $\langle \tilde{Y} \rangle = \langle \hat{\Pi} \rangle = \text{Tr}[\hat{\rho}^{(A)} \hat{\rho}^{(B)}]$. If we want to estimate the overlap within an additive error $\epsilon > 0$ with probability at least $1 - \delta$, this can be written as

$$\Pr\left(|\tilde{Y} - \langle \tilde{Y} \rangle| \geq \epsilon\right) = \Pr\left(\left|\sum_{k=1}^N x_k - \left\langle \sum_{k=1}^N x_k \right\rangle\right| \geq N\epsilon\right) \leq \delta. \quad (\text{S23})$$

Using Hoeffding's inequality, we have $\delta \geq 2e^{-\frac{N\epsilon^2}{2}}$, which means the sample complexity is

$$N = 2\epsilon^{-2} \log(2\delta^{-1}), \quad (\text{S24})$$

thus completing the proof. \square

If we give the success probability a number, e.g. $1 - \delta = \frac{2}{3}$, then this is $N = 2 \log(6)\epsilon^{-2} \approx 3.58\epsilon^{-2}$. Adopting the big- O notation for asymptotic scaling, the sample complexity simplifies to $N = O(\epsilon^{-2})$.

C. Optimality

The $N = O(\epsilon^{-2})$ sample complexity is, in fact, optimal up to a constant. A proof is given by Ref. [20, 61] for DV systems, but is easily extended to arbitrary photonic states. For completeness, we detail the proof in this section, after formally restating the result from Theorem 2 in the main text. The proof works by converting the overlap estimation problem into a decisional problem of quantum state discrimination, whose success probability is bounded by Helstrom's bound [35].

Theorem S2. (Theorem 2 of main text.) *Given the N -copy state, $(\rho^{(A)} \otimes \rho^{(B)})^{\otimes N}$, and some constants $\epsilon, \delta \in (0, \frac{1}{2})$, if an algorithm estimates $\text{Tr}[\rho^{(A)} \rho^{(B)}]$ to within additive error ϵ with success probability at least $1 - \delta$, then $N = \Omega\left(\epsilon^{-2} \left(\frac{1}{2} - \delta\right)^2\right)$.*

Proof. We consider two orthogonal basis states $|\phi_0\rangle, |\phi_1\rangle$, such that $\langle \phi_1 | \phi_0 \rangle = 0$. For some $\epsilon > 0$, we define two pure states, $\hat{\rho}_{\pm}$, that can be decomposed in terms of $|\phi_0\rangle, |\phi_1\rangle$:

$$\hat{\rho}_- = |\psi_-\rangle\langle\psi_-|, \quad \text{for } |\psi_-\rangle = \sqrt{\frac{1}{2} - \epsilon}|\phi_0\rangle + \sqrt{\frac{1}{2} + \epsilon}|\phi_1\rangle, \quad (\text{S25})$$

$$\hat{\rho}_+ = |\psi_+\rangle\langle\psi_+|, \quad \text{for } |\psi_+\rangle = \sqrt{\frac{1}{2} + \epsilon}|\phi_0\rangle + \sqrt{\frac{1}{2} - \epsilon}|\phi_1\rangle, \quad (\text{S26})$$

which satisfy

$$\text{Tr}[\hat{\rho}_- |\phi_0\rangle\langle\phi_0|] = \frac{1}{2} - \epsilon, \quad \text{Tr}[\hat{\rho}_+ |\phi_0\rangle\langle\phi_0|] = \frac{1}{2} + \epsilon. \quad (\text{S27})$$

In a quantum state discrimination problem, Alice picks and prepares one state from $\hat{\sigma}_-^{\otimes N} = (\hat{\rho}_- \otimes |\phi_0\rangle\langle\phi_0|)^{\otimes N}$ or $\hat{\sigma}_+^{\otimes N} = (\hat{\rho}_+ \otimes |\phi_0\rangle\langle\phi_0|)^{\otimes N}$ with equal prior probability, and sends it to Bob. If an algorithm described in Theorem S2 exists, then Bob can discriminate between the two non-orthogonal states, $\hat{\sigma}_\pm^{\otimes N}$, with at least $1 - \delta$ probability.

Therefore, we convert the question of lower bounding the overlap estimation problem's sample complexity to upper bounding a quantum state discrimination problem's success probability. The latter question can be answered by the Helstrom's bound [35] (or [62] for a textbook description):

$$1 - \delta \leq P_{\text{success}} \leq \frac{1}{2} \left(1 + \frac{1}{2} \|\hat{\sigma}_-^{\otimes N} - \hat{\sigma}_+^{\otimes N}\|_1 \right), \quad (\text{S28})$$

for trace distance,

$$\begin{aligned} \|\hat{\sigma}_-^{\otimes N} - \hat{\sigma}_+^{\otimes N}\|_1 &= \text{Tr} \left[\sqrt{(\hat{\sigma}_-^{\otimes N} - \hat{\sigma}_+^{\otimes N})^\dagger (\hat{\sigma}_-^{\otimes N} - \hat{\sigma}_+^{\otimes N})} \right] \\ &\leq 2\sqrt{1 - \text{Tr} [\hat{\sigma}_-^{\otimes N} \hat{\sigma}_+^{\otimes N}]} \\ &= 2\sqrt{1 - |\langle\psi_+|\psi_-\rangle|^{2N}} = 2\sqrt{1 - (1 - 4\epsilon^2)^N} \leq 4\epsilon\sqrt{N}, \end{aligned} \quad (\text{S29})$$

where in the second line we used the relationship between trace distance and trace overlap [62], and in the last line we used the fact that $(1 - 4\epsilon^2)^N \geq 1 - 4N\epsilon^2$ for $0 < \epsilon < \frac{1}{2}$ by Bernoulli's inequality. Combining Equations S28 and S29, Helstrom's bound stipulates $N \geq \epsilon^{-2} (\frac{1}{2} - \delta)^2$. \square

If we give the success probability a number, e.g. $1 - \delta = \frac{2}{3}$, then the lower bound is explicitly $N \geq \epsilon^{-2}/36 \approx 0.0278\epsilon^{-2}$. Within the asymptotic big- Ω notation, the lower bound is equivalent to the sample complexity of Theorem 1 in main text, $N = \Omega(\epsilon^{-2})$, thereby proving the scheme by BSs and PNRDs achieve the optimal complexity up to a constant scaling.

For any method that solves the overlap estimation problem, the special states we defined above, $\hat{\sigma}_\pm^{\otimes N}$, constitute worst-case instances where the method cannot guarantee a sample complexity better than $N = O(\epsilon^{-2})$ without violating the Helstrom's bound. Therefore, the sample complexity provided by our joint overlap estimation method is optimal up to a constant scaling within the big- O notation.

Note that throughout the proof for Theorem S2, no assumptions were made on the type of measurements, which can include any arbitrary combination of multi-copy, entangling or adaptive measurements. The fact that our joint overlap estimation scheme achieves the optimal scaling by use of just linear optics and PNRDs is a further advantage.

The proof was originally given in Ref. [20] for proving the optimality of the swap test in DV systems. In CV systems, the pure states $|\phi_0\rangle, |\phi_1\rangle$ can be the squeezed vacuum state and the single-photon-subtracted squeezed vacuum state, which satisfy the orthogonality condition.

III. DISTRIBUTED OVERLAP ESTIMATION

To the best of our knowledge, no rigorous sample complexity lower bound exists for distributed overlap estimation for photonic states (including CV states). We formally define the distributed overlap estimation problem, and then derive a possible method based on Monte-Carlo integration.

Problem S3. Distributed overlap estimation. *Alice is given some N -copy state $(\hat{\rho}^{(A)})^{\otimes N}$, and Bob is given $(\hat{\rho}^{(B)})^{\otimes N}$. Given some error $\epsilon \in (0, \frac{1}{2})$, their goal is to estimate $\text{Tr} [\hat{\rho}^{(A)} \hat{\rho}^{(B)}]$ to within additive error ϵ with success probability at least $2/3$ by only local quantum operations and classical communication (LOCC).*

For DV states $\hat{\rho}^{(A/B)}$ acting on d -dimensional Hilbert space, Ref. [20] proved a rigorous lower bound $N = \Omega(\max(\epsilon^{-2}, \sqrt{d}\epsilon^{-1}))$, even if adaptive multi-copy measurements and arbitrary rounds of classical communication are allowed. The proof works by converting the distributed overlap estimation problem into a decisional problem, similar to what we have done in the previous section.

The decisional problem of distributed overlap estimation problem can be described as follows: Alice has a d -dimensional Haar random state, $\hat{\rho}$, and Bob with equal prior probability either has the same state $\hat{\rho}$ or an independent d -dimensional Haar random state, $\hat{\sigma}$. Locally, Alice and Bob cannot tell the difference between the two situations. However, if Alice and Bob can solve the distributed overlap estimation problem by LOCC, then they can discriminate which situation they are in with high probability. This is because if Bob also has the same $\hat{\rho}$, then their overlap is 1,

whereas if Bob has a different $\hat{\sigma}$, the overlap scales as $1/d$. Ref. [20] proves an upper bound for the success probability of this decisional problem, which lower bounds the sample complexity of the distributed overlap estimation problem.

It is not immediately obvious how to extend the proof in Ref. [20] to CV systems. However, since energy-constrained CV states are approximately DV states, we conjecture that the same curse of dimensionality equally applies to CV systems.

In what follows, we consider a method for distributed overlap estimation on CV states in a special case when CV states are easy to learn. Our methods serve to upper bound the sample complexity for energy-constrained CV states. We leave the proof of rigorous lower bound for future work.

As shown in Equation S15, the overlap between two CV states are given by the overlap integral of their characteristic functions. Therefore, our method works by estimating the characteristic functions of the two states, $\chi^{(A/B)}(\boldsymbol{\alpha})$, at L points in phase space, before performing Monte-Carlo integration of the estimated values to estimate the overlap.

In general, learning the characteristic function of CV states is inefficient. Ref [27] proved that in the worst-case, estimation of $\chi^{(A/B)}(\boldsymbol{\alpha})$, even at just one point in phase space and allowing multi-copy entangling measurements, requires at least an exponential number of copies of the state. Therefore by extension, any general distributed overlap estimation algorithm by individually learning the characteristic functions must also require exponential sample complexity.

However, for a special case of self-reflective states, learning their characteristic function can be efficient. These types of states are defined as follows [27, 37]:

Definition S4. An M -mode state $\hat{\rho}$ with characteristic function $\chi(\boldsymbol{\alpha})$ is self-reflective if there exists some symmetric unitary matrix $\mathbf{U} \in \mathbb{C}^{M \times M}$ such that $\chi(\boldsymbol{\alpha}) = \chi(\mathbf{U}\boldsymbol{\alpha}^*)$.

The symmetric unitary matrix \mathbf{U} defines a set of axes in phase space that passes through the origin point, against which the state is reflected. For a state with reflection symmetry, there exists some set of axes against which the reflection is the state itself. A large class of interesting CV states are self-reflective, such as coherent states, squeezed states, Fock states, Gottesman-Kitaev-Preskill (GKP) states and Schrödinger cat states [27, 37]. However, there are also simple states that do not exhibit reflection symmetry, such as displaced squeezed states whose displacement axis and squeezing axis do not align.

For self-reflective states, Ref. [37] proved the following lemma for efficient learning:

Lemma S5. (Theorem 1 of Ref [37].) For a self-reflective state $\hat{\rho}$ with characteristic function $\chi(\boldsymbol{\alpha})$, given $\hat{\rho}^{\otimes N}$, L points in phase space, $\{\boldsymbol{\alpha}_i\}_{i=1}^L$, and some $\tilde{\epsilon}, \tilde{\delta} \in (0, \frac{1}{2})$, the values of $\{\chi(\boldsymbol{\alpha}_i)\}_{i=1}^L$ can be estimated to within additive error $\tilde{\epsilon}$ with success probability at least $1 - \tilde{\delta}$ for sample complexity $N = O\left(\tilde{\epsilon}^{-4} \log(L/\tilde{\delta})\right)$.

Lemma S5 overcomes the first obstacle of efficient characteristic function learning. In fact, it enables estimation of the characteristic function at exponential number of points in phase space using only a polynomial number of measurements.

A second obstacle is that the functions $\chi^{(A/B)}(\boldsymbol{\alpha})$ are theoretically defined over an infinite phase space, making Monte-Carlo integration impossible. However, in physical relevant contexts, the CV states are invariably bounded by energy, which makes it possible to evaluate the overlap integral in Equation S15 within a finite volume of phase space. We make the assumption that the functions $\chi^{(A/B)}(\boldsymbol{\alpha})$ are only important for $|\boldsymbol{\alpha}|^2 \leq \kappa M$, where M is the mode number and κ is an energy constraint per mode, inspired by similar techniques in theoretical quantum optics literature [27, 36, 37].

To be more specific, we assume that the overlap is bounded within a $2M$ -dimensional hypersphere in phase space that has radius $|\boldsymbol{\alpha}| = \sqrt{\kappa M}$, such that:

$$\left| \frac{1}{\pi^M} \int_{|\boldsymbol{\alpha}|^2 \geq \kappa M} d^{2M} \boldsymbol{\alpha} \chi^{(A)}(\boldsymbol{\alpha}) \chi^{(B)}(-\boldsymbol{\alpha}) \right| \leq \frac{\epsilon}{2}. \quad (\text{S30})$$

If we denote the hypersphere as \mathcal{A} , its volume is given by the hypersphere volume formula:

$$|\mathcal{A}| = \int_{|\boldsymbol{\alpha}|^2 \leq \kappa M} d^{2M} \boldsymbol{\alpha} = \frac{(\pi \kappa M)^M}{M!} = O\left(\frac{(e\pi\kappa)^M}{\sqrt{2\pi M}}\right), \quad (\text{S31})$$

where the asymptotic scaling is derived by using the Stirling's approximation.

Therefore, we devise the following method to solve the distributed overlap estimation problem, if the states are *a priori* known to be self-reflective:

1. Alice select L points in the hypersphere \mathcal{A} , $\{\boldsymbol{\alpha}_i\}_{i=1}^L$, that satisfy $|\boldsymbol{\alpha}_i|^2 \leq \kappa M$, and communicates the selection to Bob.

2. Alice and Bob each uses Lemma S5 to learn estimates to the characteristic function of their respective state, $\tilde{\chi}^{(A/B)}$, such that

$$\Pr \left[\bigcup_{i=1}^L \left| \tilde{\chi}^{(A)}(\boldsymbol{\alpha}_i) - \chi^{(A)}(\boldsymbol{\alpha}_i) \right| \geq \tilde{\epsilon} \right] \leq \tilde{\delta}, \quad \text{and} \quad \Pr \left[\bigcup_{i=1}^L \left| \tilde{\chi}^{(B)}(-\boldsymbol{\alpha}_i) - \chi^{(B)}(-\boldsymbol{\alpha}_i) \right| \geq \tilde{\epsilon} \right] \leq \tilde{\delta}. \quad (\text{S32})$$

3. They approximate the overlap expression in Equation S15 using the unbiased estimator \tilde{Y} , defined as

$$\tilde{Y} = \frac{|\mathcal{A}|}{\pi^M L} \sum_{i=1}^L \tilde{\chi}^{(A)}(\boldsymbol{\alpha}_i) \tilde{\chi}^{(B)}(-\boldsymbol{\alpha}_i). \quad (\text{S33})$$

Using techniques from Ref. [37], we can bound the estimation error by,

$$\begin{aligned} \left| \tilde{Y} - \text{Tr}[\hat{\rho}^{(A)} \hat{\rho}^{(B)}] \right| &= \frac{1}{\pi^M} \left| \int_{\mathcal{C}^M} d^{2M} \boldsymbol{\alpha} \chi^{(A)}(\boldsymbol{\alpha}) \chi^{(B)}(-\boldsymbol{\alpha}) - \frac{|\mathcal{A}|}{L} \sum_{i=1}^L \tilde{\chi}^{(A)}(\boldsymbol{\alpha}_i) \tilde{\chi}^{(B)}(-\boldsymbol{\alpha}_i) \right| \\ &\leq \frac{1}{\pi^M} \left| \int_{\mathcal{A}} d^{2M} \boldsymbol{\alpha} \chi^{(A)}(\boldsymbol{\alpha}) \chi^{(B)}(-\boldsymbol{\alpha}) - \frac{|\mathcal{A}|}{L} \sum_{i=1}^L \tilde{\chi}^{(A)}(\boldsymbol{\alpha}_i) \tilde{\chi}^{(B)}(-\boldsymbol{\alpha}_i) \right| + \frac{\epsilon}{2} \\ &\leq \frac{1}{\pi^M} \left| \int_{\mathcal{A}} d^{2M} \boldsymbol{\alpha} \chi^{(A)}(\boldsymbol{\alpha}) \chi^{(B)}(-\boldsymbol{\alpha}) - \frac{|\mathcal{A}|}{L} \sum_{i=1}^L \chi^{(A)}(\boldsymbol{\alpha}_i) \chi^{(B)}(-\boldsymbol{\alpha}_i) \right| \\ &\quad + \frac{|\mathcal{A}|}{L \pi^M} \left| \sum_{i=1}^L \left[\chi^{(A)}(\boldsymbol{\alpha}_i) \chi^{(B)}(-\boldsymbol{\alpha}_i) - \tilde{\chi}^{(A)}(\boldsymbol{\alpha}_i) \tilde{\chi}^{(B)}(-\boldsymbol{\alpha}_i) \right] \right| + \frac{\epsilon}{2} \end{aligned} \quad (\text{S34})$$

The first term in the last line is the estimation error in Monte-Carlo integration, given by $\frac{\sigma_L |\mathcal{A}|}{\pi^M \sqrt{L}}$, where σ_L is the population variance estimated by the sample variance:

$$(\sigma_L)^2 = \frac{1}{L-1} \sum_{i=1}^L \left[\chi^{(A)}(\boldsymbol{\alpha}_i) \chi^{(B)}(-\boldsymbol{\alpha}_i) - \frac{1}{L} \left(\sum_{j=1}^L \chi^{(A)}(\boldsymbol{\alpha}_j) \chi^{(B)}(-\boldsymbol{\alpha}_j) \right) \right]^2. \quad (\text{S35})$$

As long as this error remains finite, the Monte-Carlo integration error decreases monotonically as $1/\sqrt{L}$. However, in experiment we do not know the true function values, and therefore can only approximate the variance by the estimated function values:

$$(\tilde{\sigma}_L)^2 = \frac{1}{L-1} \sum_{i=1}^L \left[\tilde{\chi}^{(A)}(\boldsymbol{\alpha}_i) \tilde{\chi}^{(B)}(-\boldsymbol{\alpha}_i) - \frac{1}{L} \left(\sum_{j=1}^L \tilde{\chi}^{(A)}(\boldsymbol{\alpha}_j) \tilde{\chi}^{(B)}(-\boldsymbol{\alpha}_j) \right) \right]^2. \quad (\text{S36})$$

The third term in the last line of Equation S34 comes from the energy constraint assumption in Equation S30.

Finally, to bound the second term in the last line of Equation S34, we note that the magnitude of the characteristic function itself is bounded by the Hölder inequality for Schatten norms:

$$|\chi(\boldsymbol{\alpha})| = \text{Tr} \left[\hat{\rho} \hat{D}(\boldsymbol{\alpha}) \right] \leq \|\hat{D}(\boldsymbol{\alpha})\|_{\infty} \|\hat{\rho}\|_1 = 1, \quad (\text{S37})$$

The operator (or spectral) norm is the largest singular value, which for a unitary operator is $\|\hat{D}(\boldsymbol{\alpha})\|_{\infty} = 1$, and the trace norm of a density matrix is $\|\hat{\rho}\|_1 = 1$. This allows us to write,

$$\begin{aligned} &\left| \sum_{i=1}^L \left[\chi^{(A)}(\boldsymbol{\alpha}_i) \chi^{(B)}(-\boldsymbol{\alpha}_i) - \tilde{\chi}^{(A)}(\boldsymbol{\alpha}_i) \tilde{\chi}^{(B)}(-\boldsymbol{\alpha}_i) \right] \right| \\ &\leq \left| \sum_{i=1}^L \chi^{(A)}(\boldsymbol{\alpha}_i) \left[\chi^{(B)}(-\boldsymbol{\alpha}_i) - \tilde{\chi}^{(B)}(-\boldsymbol{\alpha}_i) \right] \right| + \left| \sum_{i=1}^L \left[\chi^{(A)}(\boldsymbol{\alpha}_i) - \tilde{\chi}^{(A)}(\boldsymbol{\alpha}_i) \right] \tilde{\chi}^{(B)}(-\boldsymbol{\alpha}_i) \right| \\ &\leq \left| \sum_{i=1}^L \left[\chi^{(B)}(-\boldsymbol{\alpha}_i) - \tilde{\chi}^{(B)}(-\boldsymbol{\alpha}_i) \right] \right| \max \left(\left| \chi^{(A)}(\boldsymbol{\alpha}_i) \right| \right) + \left| \sum_{i=1}^L \left[\chi^{(A)}(\boldsymbol{\alpha}_i) - \tilde{\chi}^{(A)}(\boldsymbol{\alpha}_i) \right] \right| \max \left(\left| \tilde{\chi}^{(B)}(-\boldsymbol{\alpha}_i) \right| \right) \\ &\leq 2L\tilde{\epsilon} \end{aligned} \quad (\text{S38})$$

This inequality holds with probability at least $1 - 2\tilde{\delta}$ by applying the union bound on Equation S32.

Combining all three terms in Equation S34, and if we require the overlap estimator to be within ϵ additive error with probability at least $1 - \delta$, we have:

$$\epsilon \approx \frac{\tilde{\sigma}_L |\mathcal{A}|}{\sqrt{L} \pi^M} + \frac{2|\mathcal{A}| \tilde{\epsilon}}{\pi^M} + \frac{\epsilon}{2}, \quad \delta = 2\tilde{\delta}, \quad (\text{S39})$$

where \approx is used because $\tilde{\sigma}_K$ is used to estimate the Monte Carlo estimation error. The distributed overlap estimation problem is solved if we choose:

$$\tilde{\epsilon} = \frac{\pi^M}{8|\mathcal{A}|} \epsilon, \quad L = \left(\frac{4\tilde{\sigma}_L |\mathcal{A}|}{\pi^M \epsilon} \right)^2, \quad \tilde{\delta} = \frac{1}{2} \delta. \quad (\text{S40})$$

If we substitute this into the sample complexity of Lemma S5, we get sample complexity,

$$\begin{aligned} N &= O\left(\tilde{\epsilon}^{-4} \log(L/\tilde{\delta})\right) = O\left(\epsilon^{-4} \left(\frac{|\mathcal{A}|}{\pi^M}\right)^4 \log\left(\left(\frac{|\mathcal{A}|}{\pi^M}\right)^2 \tilde{\sigma}_L^2 \epsilon^{-2} \delta^{-1}\right)\right) \\ &= O\left(\epsilon^{-4} \left(\frac{(e\kappa)^M}{\sqrt{M}}\right)^4 \log\left(\left(\frac{(e\kappa)^M}{\sqrt{M}}\right)^2 \tilde{\sigma}_L^2 \epsilon^{-2} \delta^{-1}\right)\right) \end{aligned} \quad (\text{S41})$$

where in the last line we substituted the hypersphere formula for $|\mathcal{A}|$.

Formally, we have the following result:

Theorem S6. *For distributed overlap estimation on self-reflective states, $\hat{\rho}^{(A)}$ and $\hat{\rho}^{(B)}$, given N copies of each state respectively and $\epsilon, \delta \in (0, \frac{1}{2})$, if the states satisfy*

$$\left| \frac{1}{\pi^M} \int_{|\alpha|^2 \geq \kappa M} d^{2M} \alpha \chi^{(A)}(\alpha) \chi^{(B)}(-\alpha) \right| \leq \frac{\epsilon}{2}$$

for some energy constraint $\kappa > 0$, then Alice and Bob can compute the following estimator by LOCC,

$$\tilde{O} = \frac{(\kappa M)^M}{M!} L^{-1} \sum_{i=1}^L \tilde{\chi}^{(A)}(\alpha_i) \tilde{\chi}^{(B)}(-\alpha_i),$$

which satisfies $\Pr\left[\left|\tilde{O} - \text{Tr}[\hat{\rho}^{(A)} \hat{\rho}^{(B)}]\right| \gtrsim \epsilon\right] \leq \delta$, where \sim comes from the approximation of Monte-Carlo integration error, if

$$N = O\left(\epsilon^{-4} \left(\frac{(e\kappa)^M}{\sqrt{M}}\right)^4 \log\left(\left(\frac{(e\kappa)^M}{\sqrt{M}}\right)^2 \tilde{\sigma}_L^2 \epsilon^{-2} \delta^{-1}\right)\right).$$

Therefore, if $\kappa \geq e^{-1}$, this is still an exponential sample complexity, despite the efficient protocol for learning $\chi^{(A/B)}(\alpha)$ themselves.

SIV. PHOTON SOURCE

Our experimental apparatus consists of three major components: a spontaneous parametric downconversion (SPDC) photon source, a chip-based photonic circuit and eight superconducting nanowire single-photon detectors (SNSPDs) for photon detection. In this section we give an overview of the photon source, before focusing in the next section on the details of the photonic chip.

Our SPDC source consists of a periodically-poled potassium titanyl phosphate (ppKTP) waveguide pumped by Spectra-Physics Mai Tai, a femtosecond, wideband, mode-locked Ti:Sapphire Laser. The pump pulses have repetition rate of 80 MHz. The spectrum of the pump pulses are filtered to 775 ± 0.9 nm full-width half-maximum using a pair of 3 nm bandpass filters (Thorlabs FBH780-3). The type-II SPDC process on the ppKTP waveguide (AdvR Inc.) generates a pair of collinear, orthogonally polarised signal and idler modes at 1550 nm. After the pump field is removed by a dichroic mirror followed by optical spectral filters, the signal and idler modes are separated by a

polarising beamsplitter (PBS) and coupled into polarisation-maintaining (PM) fibres, which are connected to the photonic chip. The output from the photonic chip are sent by single-mode fibres into 8 SNSPDs for photon detection.

The signal and idler modes form a two-mode squeezed vacuum (TMSV) state, which can be described by

$$|\text{TMSV}\rangle = \sqrt{1 - |\lambda|^2} \sum_{n=0}^{\infty} \lambda^n |n\rangle_s |n\rangle_i, \quad (\text{S42})$$

where λ is a parameter that depends on the pump field and the ppKTP crystal, and subscripts s, i are used to denote the signal and idler modes.

In our experiment, we keep the pump field low at $65\mu\text{W}$. The total coincidence rate between the signal and idler modes, sent through the photonic chip and detected on SNSPDs, is measured to be 5500 coincidences per second. To measure the higher photon number events, we utilise a Hanbury Brown and Twiss style interferometer. We block either signal or idler mode, and split the other mode on a balanced beamsplitter before detection on SNSPDs. The coincidence rate measures the probability of having $|n\rangle_s |n\rangle_i$ components with $n \geq 2$ in Equation S42. At the current pump intensity, we measure this coincidence rate to be lower than 50 per second.

Neglecting the low-rate high-photon-number events, our SPDC source can approximate a probabilistic two-photon source. During the experiment, we only post-select outcomes where two photons are measured on the detectors. By this post-selection, we can also remove the effects of photon loss in the experiment.

The indistinguishability of our two-photon source is measured by a Hong-Ou-Mandel (HOM) sweep. The fibre coupler for the signal mode is placed on top of a piezo-electric translation stage. The signal and idler modes are interfered on a balanced beamsplitter implemented on the photonic chip. The output coincidences are measured against translation stage position. The visibility, $V = (P_{\max} - P_{\min})/P_{\max}$, of the HOM dip was measured to be 95.40%, as shown in Fig. S1.

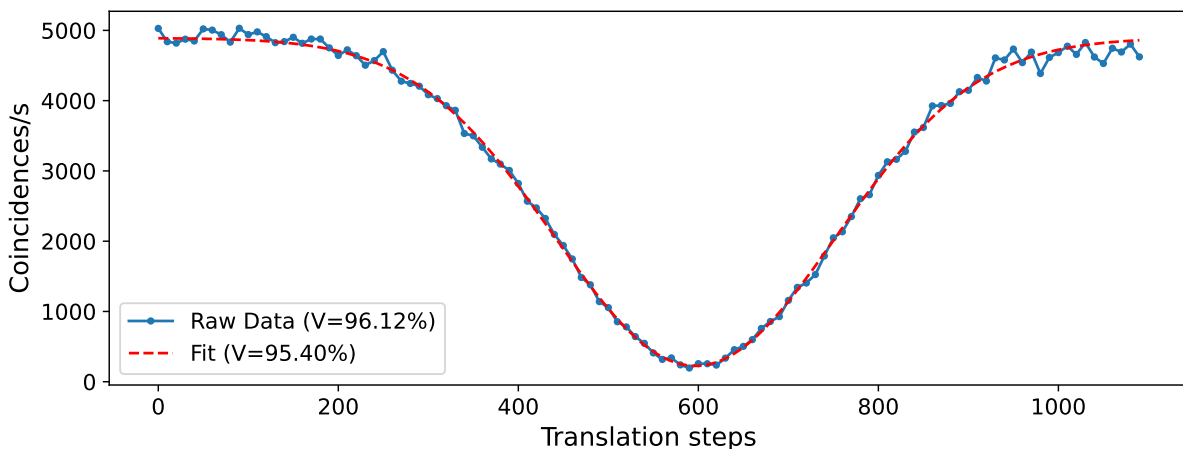


FIG. S1. HOM sweep result. The visibility directly calculated from the raw coincidence data differ slightly from the fitting result to a Gaussian model.

SV. PHOTONIC INTEGRATED CIRCUIT

A. Setup

The photonic integrated circuit (or chip) used in this work was fabricated by a multi-project wafer run at LioniX International BV. The TriPleX waveguide technology was used to fabricate waveguides based on alternating layers of silicon nitride and silicon dioxide [63]. A reconfigurable linear optical circuit is implemented on the chip by use of thermo-optically tunable phaseshifters. These are sections of the waveguides with refractive index that can be thermally tuned to change the relative phase that photons pick up when passing through. In our chip, a 1 mm long platinum resistor is placed on top of each phaseshifter and thermal tuning is achieved by passing current through the resistor. The power dissipation per phaseshifter is around 700 mW, or around 12 V and 60 mA, for a 2π phase shift. This adds up to 70 W maximum power consumption for a total of 100 phaseshifters on the chip, though typically in practice we operate the chip at much lower power.

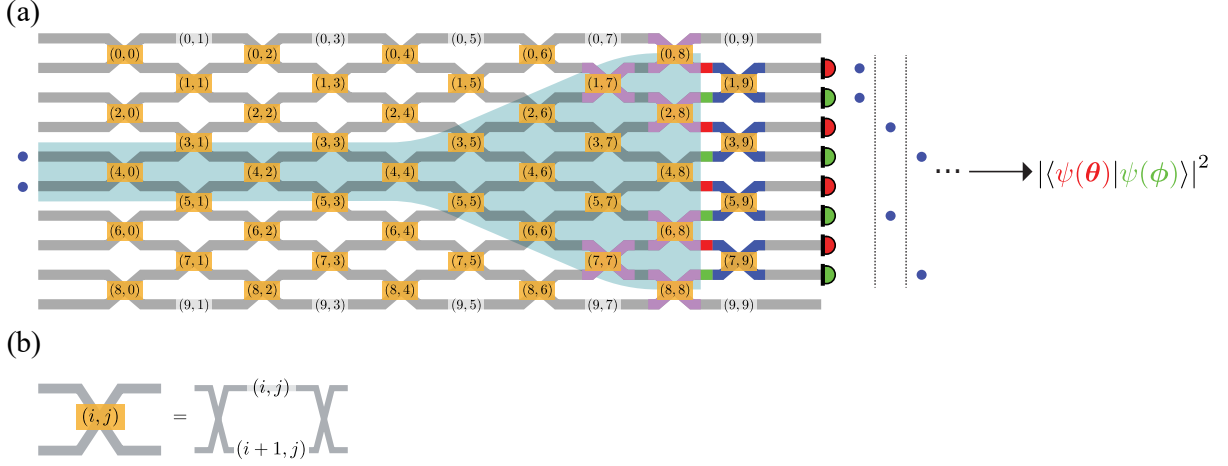


FIG. S2. (a) Labeled scheme. MZIs and phaseshifters are labelled by orange and white background boxes respectively. Grey lines are waveguides, with DCs omitted and MZIs simplified as waveguide crossings. The six MZIs for active phase encodings are coloured by purple. After column 8, one qudit state $|\psi(\theta)\rangle$ is encoded in modes 1, 3, 5, 7, coloured red; another qudit state $|\psi(\phi)\rangle$ is encoded in modes 2, 4, 6, 8, coloured green. The two qudit states are interfered mode-wise on four MZIs that implement balanced beamsplitters on column 9, coloured blue. The output is measured by eight SNSPDs on modes 1 to 8. The output coincidence distribution directly estimates the state overlap. (b) Layout of a symmetric MZI labelled (i, j) , with internal phaseshifters labelled (i, j) and $(i + 1, j)$.

The chip is optically packaged with polarisation-maintaining (PM) fibre arrays for both input and output coupling, provided by PHIX Photonics Assembly BV. Light is coupled from these fibre arrays into the chip by edge coupling. Coupling efficiency is measured to be as high as 88% per facet. The end-to-end transmission varies between different input and output modes and is typically around 50%, which includes effects of propagation loss and coupling loss.

The remaining electrical and electronic packaging was done in-house. We use a 120-channel source measurement system (XPOW-120AX-CCvCV-U by Niclslab Ops, Inc.) to supply independent voltage/current sourcing and measurement to the thermo-optical phaseshifters on the chip. We operate it in constant current mode, which has a 16-bit resolution for each channel, and set the output range per channel to 0–100 mA and 0–15 V. The system is connected to a computer via USB and is controlled by a self-written Python package for calibration and control.

The chip itself is mounted on a gold-plated copper base for thermal dissipation. Also mounted on the base is a printed circuit board for electrical connections. Inside the copper base is a thermistor for temperature sensing, which feeds back to a thermoelectric temperature controller (TEC) (Model 350B by Newport Corporation). Beneath the chip mount is a Peltier cooler and a copper heat sink. The Peltier cooler works by maintaining a constant temperature difference between its upper and lower surface. A fan is used to blow air through the copper heat sink for better heat dissipation. The TEC has maximum output power of 55 W. While slightly short of the 70 W maximum power dissipation power on chip, it suffices for the operations in this work. When in operation, we set the TEC to maintain the thermistor inside the copper base at $28.0 \pm 0.1^\circ\text{C}$ temperature.

The chip implements a 10-mode universal linear-optical interferometer that follows the Bell decomposition scheme [33]. The basic unit for control in the Bell scheme is a symmetric Mach-Zehnder Interferometer (MZI) as shown in Fig. S2(c). Each MZI consist of two directional couplers (DCs) acting as balanced beamsplitters and two internal phaseshifters in between, one on each arm.

A labelled schematic of the chip is shown in Fig. S2(a). The optical modes are labelled from 0 to 9. Each phaseshifter is labelled with a unique tuple (i, j) , where i, j run from 0 to 9, i being the row index (which is also mode index) and j being the column index. The MZIs, for convenience, share the label of their upper phaseshifter. As a result, MZI labels (i, j) must satisfy $i + j$ being an even number. In the Bell-scheme, there are standalone ‘external’ phaseshifters on alternating columns on mode 0 and 9 for full phase programmability. These are labelled as $(0, j)$ and $(9, j)$ for odd j .

B. Control

The action of an ideal phaseshifter applies some phase θ to a single optical mode, which can be represented by the transfer matrix

$$\begin{pmatrix} 1 & 0 & \cdots & & \\ 0 & \ddots & & & \\ \vdots & & e^{i\phi} & & \\ & & & \ddots & \\ & & & & 1 \end{pmatrix}. \quad (\text{S43})$$

In a thermo-optic phaseshifter, a change in temperature causes a proportionate change in refractive index depending on the thermo-optic coefficient of the material. This change is typically linear with negligible second order term [64, 65]. Therefore, we can assume a linear relationship between the dissipated electric power $P_{\text{el}} = VI$ in the resistor and the induced phase change $\Delta\theta$, i.e.

$$\Delta\theta \propto \Delta n_{\text{eff}} \propto \Delta T \propto P_{\text{el}}, \quad (\text{S44})$$

where Δn_{eff} is the change in effective refractive index of the waveguide segment, and ΔT is the change in temperature. The proportionality constant depends on the geometry of the waveguide and the material properties.

The XPOW source measurement system can measure both voltage and current. However, the voltage measurement does not accurately reflect the voltage drop across the phaseshifter due to non-zero resistance on the shared ground. Therefore, we operate the XPOW in constant current mode and only use the current measurement. While theoretically the dissipated power should be $P_{\text{el}} = I^2 R$, the resistance of the phaseshifter also changes as it heats up and becomes a function of the current. This effect is non-negligible especially since the 2π power is as high as 700 mW. Therefore, we write out the phase change as a polynomial function of the current:

$$\theta = b + k^{(2)} I^2 + k^{(3)} I^3 + \dots, \quad (\text{S45})$$

where b is the residual phase when no current is applied. Given a set of calibration data of applied current versus phase change, a polynomial fit can be used to determine the coefficients up to a cut-off. In practice, we store the raw calibration data and use numerical interpolation to determine the required current for a target phase.

The transfer matrix of a directional coupler (DC) can be written in the form of [66]

$$\begin{pmatrix} \cos(\frac{\pi}{4} + \alpha) & i \sin(\frac{\pi}{4} + \alpha) \\ i \sin(\frac{\pi}{4} + \alpha) & \cos(\frac{\pi}{4} + \alpha) \end{pmatrix}, \quad (\text{S46})$$

where α is a small error term accounting for fabrication imperfections. For an ideal balanced DC, $\alpha = 0$. The unitary transfer matrix of a symmetric MZI (Fig. S2(b)) with internal phaseshifters θ_1, θ_2 and DC errors α, β can then be derived as

$$\tilde{T}(\theta_1, \theta_2, \alpha, \beta) = \begin{pmatrix} \cos \beta & i \sin \beta \\ i \sin \beta & \cos \beta \end{pmatrix} T(\theta_1, \theta_2) \begin{pmatrix} \cos \alpha & i \sin \alpha \\ i \sin \alpha & \cos \alpha \end{pmatrix}, \quad (\text{S47})$$

where $T(\theta_1, \theta_2)$ is the ideal MZI transfer matrix (when $\alpha = \beta = 0$), given by

$$T(\theta_1, \theta_2) = i e^{i\Sigma} \begin{pmatrix} \sin \delta & \cos \delta \\ \cos \delta & -\sin \delta \end{pmatrix}, \quad (\text{S48})$$

for MZI phase $\Sigma = (\theta_1 + \theta_2)/2$ and internal phase $\delta = (\theta_1 - \theta_2)/2$. If $\theta_{1,2}$ are fully tunable in range $[0, 2\pi]$, then Σ can cover $[0, 2\pi]$ and δ can cover $[-\pi, \pi]$. The Σ and δ phase are the two degrees of freedom for reconfiguring each MZI. The rest of the text sometimes refer to them as the ‘MZI phase’ and ‘internal phase’ respectively, or simply as ‘ Σ/δ phase’.

There are three special states of the MZI, namely the ‘cross’ state, the ‘bar’ state, and the ‘balanced’ state, which correspond to setting the δ phase to $0, \frac{\pi}{2}$ or $\frac{\pi}{4}$ respectively.

Section SVD will describe the calibration scheme for the chip. The goal of the calibration is to find a mapping between the current values supplied via the XPOW unit and the phases on each phaseshifter. If all phases are fully tunable between $[0, 2\pi]$, then the rectangular mesh of phaseshifters and MZIs shown in Fig. S2(a) is sufficient to implement any arbitrary 10×10 unitary matrix up to a global phase on each mode. By adding an additional layer

of stand-alone phaseshifters on the input and output modes respectively, our chip layout would recover the universal linear optical scheme proposed in Ref. [33].

However, for linear-optical experiments where the input light is a multi-mode Fock state and the output of the circuit is directly measured by phase-insensitive photon detectors, the input and output phaseshifters do not change experimental outcome and can be omitted. In the next section, we will describe how an overlap estimation circuit is implemented on chip for our experiment.

C. Overlap estimation circuit

The overlap estimation circuit is shown in Fig. S2(a). The input are two single photons sent into modes 4 and 5 respectively (modes labelled from 0 to 9). Hence, the input state can be described by $\hat{a}_4^\dagger \hat{a}_5^\dagger |0\rangle$, where $\hat{a}_{4,5}^\dagger$ are the creation operators for the two modes.

We wish to encode two four-mode qudit states, which occupy modes 1, 3, 5, 7 and 2, 4, 6, 8 respectively, that are described by:

$$\begin{aligned} |\theta\rangle = |\psi(\theta)\rangle &= \left(A_0 \hat{a}_1^\dagger + A_1 e^{i\theta_1} \hat{a}_3^\dagger + A_2 e^{i(\theta_1+\theta_2)} \hat{a}_5^\dagger + A_3 e^{i(\theta_1+\theta_2+\theta_3)} \hat{a}_7^\dagger \right) |0\rangle, \\ &= e^{i(\theta_1+\theta_2-\frac{\pi}{2})} \left(A_0 e^{-i(\theta_1+\theta_2-\frac{\pi}{2})} \hat{a}_1^\dagger + A_1 e^{-i(\theta_2-\frac{\pi}{2})} \hat{a}_3^\dagger + A_2 e^{i\frac{\pi}{2}} \hat{a}_5^\dagger + A_3 e^{i(\theta_3+\frac{\pi}{2})} \hat{a}_7^\dagger \right) |0\rangle \\ |\phi\rangle = |\psi(\phi)\rangle &= \left(A_0 \hat{a}_2^\dagger + A_1 e^{i\phi_1} \hat{a}_4^\dagger + A_2 e^{i(\phi_1+\phi_2)} \hat{a}_6^\dagger + A_3 e^{i(\phi_1+\phi_2+\phi_3)} \hat{a}_8^\dagger \right) |0\rangle, \\ &= e^{i(\phi_1+\frac{\pi}{2})} \left(A_0 e^{-i(\phi_1+\frac{\pi}{2})} \hat{a}_2^\dagger + A_1 e^{-i\frac{\pi}{2}} \hat{a}_4^\dagger + A_2 e^{i(\phi_2-\frac{\pi}{2})} \hat{a}_6^\dagger + A_3 e^{i(\phi_2+\phi_3-\frac{\pi}{2})} \hat{a}_8^\dagger \right) |0\rangle, \end{aligned} \quad (\text{S49})$$

where we denote the qudit states as $|\theta\rangle, |\phi\rangle$ as shorthand. In the second line of each qudit expression, we extracted a global phase that can be ignored in the encoding. The result is that the phases are set relative to output modes 4 and 5, which sit in the middle of the chip. This way, we can keep MZI (4, 8) at a low power setting. This separates the actively tuned phaseshifters in column 8 and reduces the crosstalk effects.

The amplitudes $\{A_i\}_{i=0}^3$ are fixed and chosen to be

$$\begin{cases} A_0 = \sin(\varphi_1/2) \\ A_1 = \cos(\varphi_1/2) \sin(\varphi_2/2) \\ A_2 = \cos(\varphi_1/2) \cos(\varphi_2/2) \sin(\varphi_3/2) \\ A_3 = \cos(\varphi_1/2) \cos(\varphi_2/2) \cos(\varphi_3/2) \end{cases} \quad \text{for} \quad \begin{cases} \varphi_1 = 0.86231713 \\ \varphi_2 = 1.34230503 \\ \varphi_3 = 1.66199945 \end{cases}. \quad (\text{S50})$$

The values are chosen by optimising the Support Vector Machine's (SVM) classification accuracies for the three datasets in Section SVI.

In columns 0 to 8 of the chip, we implement a unitary U , such that

$$\begin{aligned} U(\theta, \phi) \left(\hat{a}_4^\dagger \hat{a}_5^\dagger |0\rangle \right) &= \left(A_0 e^{i(\frac{\pi}{2}+\phi_{(0,8)}+\phi_{(1,7)})} \hat{a}_1^\dagger + A_1 e^{i(\frac{\pi}{2}+\phi_{(2,8)}+\phi_{(1,7)})} \hat{a}_3^\dagger + A_2 e^{i\frac{\pi}{2}} \hat{a}_5^\dagger + A_3 e^{i(\frac{\pi}{2}+\phi_{(6,8)})} \hat{a}_7^\dagger \right) \\ &\quad \left(A_0 e^{i(-\frac{\pi}{2}+\phi_{(2,8)})} \hat{a}_2^\dagger + A_1 e^{-i\frac{\pi}{2}} \hat{a}_4^\dagger + A_2 e^{i(-\frac{\pi}{2}+\phi_{(6,8)}+\phi_{(7,7)})} \hat{a}_6^\dagger + A_3 e^{i(-\frac{\pi}{2}-\phi_{(8,8)}-\phi_{(7,7)})} \hat{a}_8^\dagger \right) |0\rangle. \end{aligned} \quad (\text{S51})$$

Implementation of this unitary is not unique. We adopt the circuit shown in Figure S2. In columns 0 to 4, the internal phases of MZIs on the route of the light are set to $\delta = \frac{\pi}{2}$, such that the two photons propagate almost uninterfered with each other. The internal phases of MZIs on columns 5 to 8 are set to implement the amplitude values $\{A_i\}_{i=0}^3$ in Equation S50. The MZI phases in columns 5 and 6 are set to equal on each active MZI.

The relative phases $\phi_{(i,j)}$ in Equation S51 are MZI phases relative to the column reference phase. To be more specific, the relative phase in column 8 is the $\Sigma_{(4,8)}$ phase encoded on MZI (4, 8). In Column 7, MZIs (3, 7) and (5, 7) are set to have the same Σ phase and serve as the relative phase. Hence, by tuning the MZI phases (i.e. the Σ phases) on the following six MZIs, we can encode arbitrary qudits in the form of Equation S49: MZIs (0, 8), (2, 8), (1, 7), (6, 8), (8, 8), (7, 7).

Finally, the four MZIs (1, 9), (3, 9), (5, 9), (7, 9) in column 9 are set to have internal phase $\delta = \frac{\pi}{4}$ to implement balanced beamsplitters:

$$T_{\text{balanced}} \propto \frac{1}{\sqrt{2}} \begin{pmatrix} 1 & 1 \\ 1 & -1 \end{pmatrix}. \quad (\text{S52})$$

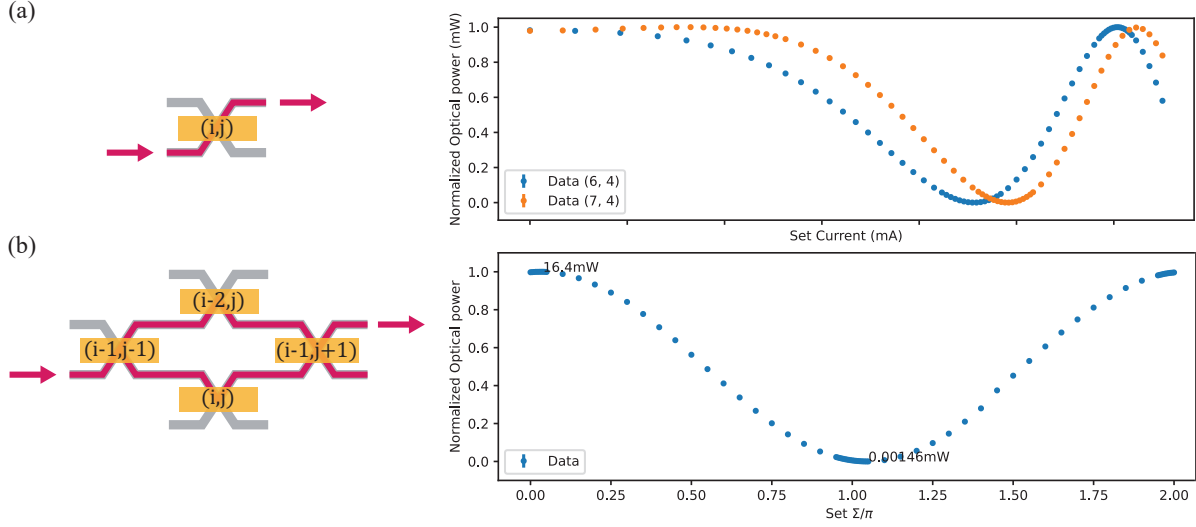


FIG. S3. (a) Calibration of internal phaseshifters and the δ phase of MZI (i, j) . (b) Calibration of the Σ phase of MZI (i, j) .

The relative π phase difference between neighbouring modes in Equation S51 evens out the input phase difference in T_{balanced} .

The output modes from 1 to 8 are connected to eight SNSPDs. We measure and post-select two-photon outputs to trace out the effects of loss. Splitting the output modes into two registers, we showed in the main text that coincidence probability across the two registers allows us to estimate the overlap between the qudit states. In our scheme, the two registers happen to be odd-number-labelled modes 1, 3, 5, 7 and even-number-labelled modes 2, 4, 6, 8. Therefore, we divide the two-photon outputs into even-parity events, i.e. coincidence events between modes k and l where $k + l$ is an even number; and odd-parity events where $k + l$ is an odd number. If we collect N total samples that measure two photons, which include N_{odd} odd-parity events, the overlap is estimated by

$$|\langle \psi(\theta) | \psi(\phi) \rangle|^2 \approx 1 - 2(1 - R) \frac{N_{\text{odd}}}{N}, \quad (\text{S53})$$

where $R = \sum_{i=0}^3 A_i^4 < 1$. This equals the bunching probability, or probability of having two photons in the same output mode that cannot be distinguished by click detectors such as SNSPDs. If photon-number resolving detectors (PNRDs) were used, then we do not need this rescaling factor.

D. Calibration

The goal of calibration is to find a mapping between the current values applied to the electric channels and the phase values of each MZI and phaseshifter.

For an MZI described by Equation S47, if we send a coherent state with unit intensity into the lower input mode, then power in the upper output mode is:

$$P = \sin^2(\beta - \alpha) + \frac{\cos^2(\beta + \alpha) - \sin^2(\beta - \alpha)}{2} (\cos(\theta_1 - \theta_2) + 1). \quad (\text{S54})$$

We label the two internal phaseshifters as (i, j) and $(i + 1, j)$, and express the internal phases as

$$\theta_{i,j} = \Delta_{i,j}(I_{i,j}) + b_{i,j}, \quad \theta_{i+1,j} = \Delta_{i+1,j}(I_{i+1,j}) + b_{i+1,j}, \quad (\text{S55})$$

where b is the residual phase when no current is applied, and $\Delta(I)$ is the phase change that is a function of the applied current I . If we sweep the current on each internal phaseshifter, the output power follows a sinusoidal curve as shown in Fig. S3(a). From this, we reconstruct the relationship between $\Delta(I)$ and I for each internal phaseshifter, as well as the residual relative phase, $b_{i,j} - b_{i+1,j}$. This enables us to set the internal δ phase of the MZI.

However, to set the Σ phase of the MZI, we also need to know $b_{i,j} + b_{i+1,j}$ relative to the next MZI in the column. To do so, we construct a ‘meta-MZI’ as shown in Fig. S3(b) using four MZIs, which are labelled $(i - 2, j)$, (i, j) , $(i -$

$1, j - 1), (i - 1, j + 1)$. The target is MZI (i, j) , which is set to bar state that fixes $\delta_{i,j} = \frac{\pi}{2}$ and leaves $\Sigma_{i,j}$ as the free parameter to be calibrated. The MZI $(i - 2, j)$ is also set to cross state, with $\delta_{i-2,j} = 0$ and $\Sigma_{i-2,j}$ fixed. The MZIs $(i - 1, j - 1)$ and $(i - 1, j + 1)$ are set to balanced states, with $\delta_{i-1,j-1} = \delta_{i-1,j+1} = \frac{\pi}{4}$ and $\Sigma_{i-1,j-1}, \Sigma_{i+1,j-1}$ arbitrary as they do not affect the output power.

If light is sent into the lower input port of MZI $(i - 1, j - 1)$, then the upper output power of MZI $(i - 1, j + 1)$ can be modelled as

$$P = a + c \cos(\Sigma_{i,j} - \Sigma_{i-2,j} + \xi) \quad (\text{S56})$$

where a, c are constants that depend on the errors of the effective DCs as well as input power, channel efficiency and detector efficiency. The phase ξ is an error term that's due to the DC errors inside MZI $(i - 1, j - 1)$ and MZI $(i - 1, j + 1)$. Imperfect DCs inside an MZI results in a small relative phase between its two outputs, which become a phase error in the meta-MZI. By sweeping the relative MZI phase, $\Sigma_{(i,j)} - \Sigma_{(i-2,j)}$, we get a sinusoidal output power curve as shown in Fig. S3(b), whose offset phase estimates the relative residual phase $b_{i,j} + b_{i+1,j} - b_{i-2,j} - b_{i-1,j}$. This enables Σ phase tuning on MZI (i, j) .

Additionally, we can also calibrate the directional coupler errors of the chip from the visibilities of the sinusoidal sweeps. Among the active MZIs used in this experiment, the median splitting ratio of directional couplers is 52.8 : 47.2.

Relative channel efficiencies can be estimated by directing light into different output modes by setting the appropriate MZIs and comparing the output power, accounting for the MZI encoding errors.

Finally, crosstalk effects between MZIs were calibrated by repeating calibrations at various phase settings of neighbouring MZIs. The calibration results can be interpolated to reconstruct a look-up table that describes phase changes due to crosstalk for each location and and source of crosstalk.

After calibration, the resulting circuit fidelity is shown in Fig. S4. Fig. S4(a) shows the fidelity of the output coincidence distribution: $F = \sum_{(i,j)} \sqrt{\frac{P_{(i,j)}^{(\text{ideal})}}{P_{(i,j)}^{(\text{exp})}}}$, where $P_{(i,j)}$ is the coincidence probability between modes i and j , and superscripts (ideal) and (exp) indicate ideal calculations and experimental estimates, respectively. The average fidelity is 0.980 ± 0.006 across the experiments conducted in this work.

The resulting overlap estimation accuracy is visualised in Fig. S4(b). As is clear from the fidelity values as well as the overlap values, there is still room for improvement in the calibration scheme, especially for better crosstalk mitigation.

E. Simulator

We also designed a simple simulator that emulates the thermal crosstalk between phaseshifters. The single-phaseshifter sweeps in the previous section returns a phase-current relationship. If we set a phase according to this relationship, the phase value would be proportional to the local electric heat, but does not take into account any heat dissipation to neighbouring phaseshifters. If we denote the phase we set onto the phaseshifter (i, j) according to single phaseshifter calibration result as $\tilde{\theta}_{i,j}$, and the actual phase change induced on the phaseshifter as $\theta_{i,j}$, then we use a simple mathematical relationship to emulate the crosstalk effect:

$$\theta_{i,j} = \tilde{\theta}_{i,j} + \left(\sum_{l,m=0}^9 K_{(i,j),(l,m)} \tilde{\theta}_{l,m} \right) \left(1 + \eta_{i,j} \tilde{\theta}_{i,j} \right) + \epsilon_{i,j}, \quad (\text{S57})$$

where $K_{(i,j),(l,m)}$ is a coefficient that quantifies the proportion of heat leaked from phaseshifter (l, m) to phaseshifter (i, j) , $\eta_{i,j}$ is a coefficient that we use to capture any non-linear crosstalk effects, and $\epsilon_{i,j}$ is a calibration error term.

Theoretically, the summation term in Equation S57 should be over all phaseshifters (l, m) . Practically, the K coefficients should decay according to geometric distance. We model the coefficients as follows:

$$K_{(i,j),(l,m)} = \begin{cases} K^{(1)} \xi_{(i,j),(l,m)} & \text{if nearest neighbour,} \\ K^{(2)} \xi_{(i,j),(l,m)} & \text{if second-nearest neighbour,} \\ K^{(3)} \xi_{(i,j),(l,m)} & \text{if third-nearest neighbour,} \\ K^{(4)} \xi_{(i,j),(l,m)} & \text{otherwise,} \end{cases} \quad (\text{S58})$$

where $K^{(1,2,3,4)}$ are the baseline crosstalk coefficients for nearest, second-nearest, third-nearest neighbour (according to the phaseshifters' geometric layout on chip) and global crosstalk respectively, and ξ is a normal distributed random value with mean 1 and standard deviation 0.05, i.e. $\xi \sim \mathcal{N}(1, 0.05)$. This simplifies the number of parameters in our simulator while also keeping variance between phaseshifters.

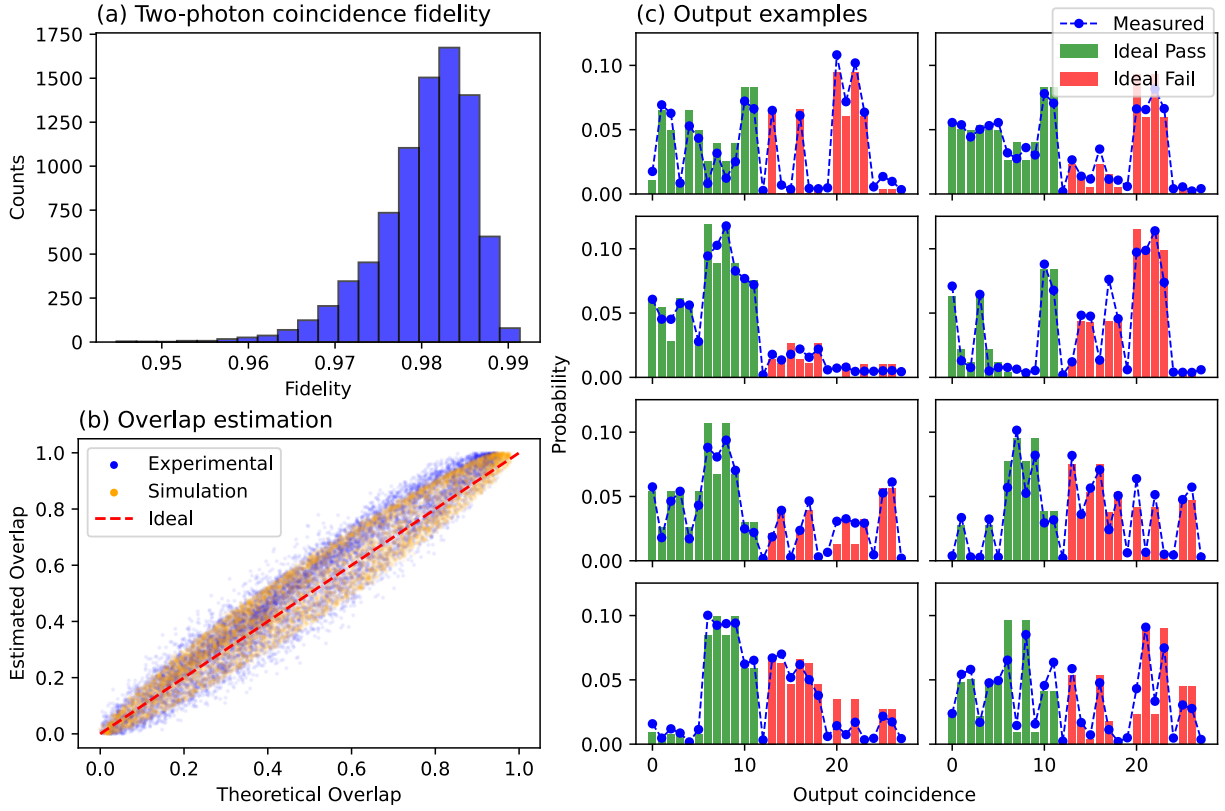


FIG. S4. (a) Fidelity of the output coincidence distribution. Data in this figure are taken from the classification experiment for overlapping blobs dataset. (b) Scatter plot of experimentally estimated and simulated overlap values against theoretical overlap values. (c) Example output coincidence distributions for eight random circuit encodings. Green bars represent even-parity coincidence outcomes, denoted ‘Pass’. Red bars represent odd-parity coincidence outcomes, denoted ‘Fail’. Blue dashed line plots the experimentally measured output distribution.

Experimental tests revealed that the crosstalk behaviour on our chip between two phaseshifters, (l, m) where the heat is initially applied to (or ‘aggressor phaseshifter’), and (i, j) where the heat dissipates to (or ‘victim phaseshifter’), not only depends on $\tilde{\theta}_{l,m}$ of the aggressor phaseshifter, but also on the local $\tilde{\theta}_{i,j}$ of the victim phaseshifter. This is why an additional $\eta_{i,j}$ coefficient is included to capture this non-linear behaviour. Typically, this coefficient is very small but non-negligible. This adds difficulty to the crosstalk calibration step described in the previous section: we have to sweep neighbouring MZIs at sufficient points in their 2π range in order to construct a look-up table that fully captures this non-linear behaviour. In the digital simulator, we model the coefficients as a Gaussian random number with mean η and standard deviation 0.1η , or $\eta_{i,j} \sim \mathcal{N}(\eta, 0.1\eta)$, where η is a common non-linear coefficient for all phaseshifters.

Finally, we model the calibration error as an additive error on the actual phase. We also set a global calibration error value, ϵ , and for each phaseshifter (i, j) , the calibration error $\epsilon_{i,j}$ is a Gaussian random value with mean $\pm\epsilon$ (with equal probability) and standard deviation 0.01 radians.

Therefore, to summarise, this simple crosstalk simulator has the following hyperparameters we can tune: $K^{(1,2,3,4)}$ for baseline crosstalk coefficients, η for baseline non-linear coefficient and ϵ for baseline calibration error. The simulator evolves the phase values we set without considering crosstalk, $\tilde{\theta}_{i,j}$, to phase values we would get if crosstalk behaves according to Equation S57. We can then simulate the output probabilities according to the input states. After rough tuning of the hyperparameters, we were able to simulate a spread of overlap errors that is similar to the experimental outcome, as shown by the orange scatter plots in Fig. S4(b). This involves setting $K^{(1)} = 1.6\%$, $K^{(2)} = 0.4\%$, $K^{(3)} = 0.16\%$, $K^{(4)} = 0.05\%$, $\eta = 1\%$, and $\epsilon = 0.02$ rad. This is the same simulator used to simulate the online learning protocol in the main text.

The crosstalk parameters are very low compared to the actual crosstalk behaviour we measured, which revealed typical values of $K^{(1)} = 8\%$, $K^{(2)} = 5\%$. This demonstrates the extent of success of our crosstalk mitigation method described in the previous section. However, the fact that we still have a non-negligible spread in the overlap values, as well as a limited fidelity in the output coincidence distribution, shows how significant the impact of thermal crosstalk

is.

Recently, machine-learning assisted routines have been proposed for high-fidelity photonic circuit calibration [67, 68]. One direction for future improvement is adopting similar routines to directly learn the parameters in Equation S57. Then we can directly infer the relationship between $\tilde{\theta}$, the phase values we set, and θ , the phase values we would actually get. Alternatively, black-box models such as neural networks or tree-based methods may also be adopted instead of the clear-box model we propose here. We leave this future work.

SVI. CLASSIFICATION BY SUPPORT VECTOR MACHINES

Firstly, we introduce the classical support vector machine (SVM) algorithm. Consider a set of data, $\{\mathbf{x}_i, y_i\}_{i=1}^m$, that consists of m samples of d -dimensional data vectors, $\mathbf{x}_i \in \mathbb{R}^d$, to each of which a binary label, $y_i = \pm 1$, is assigned. In this supplementary section, we use subscript i to label the different data instances, not to be confused with the mode label in earlier text. For now, we assume that the data are linearly separable in Euclidean space. In other words, we can find a hyperplane defined by some vector $\mathbf{w} \in \mathbb{R}^d$ and some intercept $b \in \mathbb{R}$, such that $y_i = \text{sign}(\mathbf{w}^T \mathbf{x}_i + b)$, or that $y_i(\mathbf{w}^T \mathbf{x}_i + b) - 1 \geq 0$ for all $i \in [1, m]$. The goal of SVM is to find some \mathbf{w} that maximises the separation between the two classes of data [69]. A textbook introduction of the algorithm can be found in e.g. Ref. [2].

To maximise the separation, the classification task is turned into a constraint optimisation problem:

$$\begin{aligned} & \min_{\mathbf{w}, b, \xi_i} \frac{1}{2} \|\mathbf{w}\|_2 + C \sum_{i=1}^m \xi_i \\ & \text{subject to } \xi_i \geq 0 \\ & y_i(\mathbf{w}^T \mathbf{x}_i + b) \geq 1 - \xi_i \quad \forall i \in [1, m], \end{aligned} \tag{S59}$$

where we introduced a soft-margin constraint with some slack constant C . A large C corresponds to a lower tolerance for data points to fall on the wrong side of the decision boundary. A hard constraint, with all $\xi_i = 0$, corresponds to $C = \infty$. The constrained optimisation problem can be solved by solving its Lagrangian dual program:

$$\begin{aligned} & \max_{\beta_i} \sum_{i=1}^m \beta_i - \frac{1}{2} \sum_{i=1}^m \sum_{j=1}^m \beta_i \beta_j y_i y_j \mathbf{x}_i^T \mathbf{x}_j \\ & \text{subject to } 0 \leq \beta_i \leq C \\ & \sum_{i=1}^m \beta_i y_i = 0. \end{aligned} \tag{S60}$$

To derive Equation S60 from Equation S59, we first consider the hard-constraint problem with $\xi_i = 0$. Taking Lagrange multipliers, $\beta_i > 0$, constrained optimisation of Equation S59 is equivalent to minimising the following Lagrangian without constraints:

$$\mathcal{L} = \frac{1}{2} \mathbf{w}^T \mathbf{w} - \sum_i \beta_i [y_i(\mathbf{w}^T \mathbf{x}_i + b) - 1]. \tag{S61}$$

Taking derivatives, we find,

$$\frac{\partial \mathcal{L}}{\partial \mathbf{w}} = \mathbf{w} - \sum_i \beta_i y_i \mathbf{x}_i = 0, \tag{S62}$$

$$\frac{\partial \mathcal{L}}{\partial b} = - \sum_i \beta_i y_i = 0, \tag{S63}$$

which we substitute back into the Lagrangian to recover the optimisation problem in Equation S60. Finally, if there exists some point, \mathbf{x}_i , that cannot satisfy the hard constraint, they would theoretically have infinite support in $\beta_i = \infty$. In this case, we can clip their support at some slack constant, C , which recovers the soft margin of $0 \leq \beta_i \leq C$ in Equation S60.

A key observation is that the optimisation problem now *only* depends on the inner product, $\mathbf{x}_i^T \mathbf{x}_j$, not on any individual data vectors. We can define this as a kernel function, $K(\mathbf{x}_i, \mathbf{x}_j) = \mathbf{x}_i^T \mathbf{x}_j$. If the data are no longer linearly separable in the original Euclidean space, instead of computing a non-linear classification problem, the ‘kernel trick’

is to map the data vectors into a higher-dimensional space by defining a suitable alternative kernel function and then to solve the same linear problem in the new space.

In our work, we adopt a quantum feature map, where three-dimensional unseen vectors specify phase-encoded qudits $\mathbf{x} \rightarrow |\psi(\mathbf{x})\rangle$, such that the kernel function becomes $K(\mathbf{x}_i, \mathbf{x}_j) = |\langle \psi(\mathbf{x}_i) | \psi(\mathbf{x}_j) \rangle|^2$. The data vectors \mathbf{x} represent the three phase degrees of freedom of the qudit, $\mathbf{x} = \boldsymbol{\theta}$ (Equation 3 in main text). For notational consistency, we continue to use subscript-labelled \mathbf{x}_i throughout this supplementary section, though in the main text we used superscripts instead to differentiate the data labels from the optical mode labels.

We denote the kernel function evaluations between the training data as an $m \times m$ overlap matrix \mathbf{K} , which has elements $K_{ij} = K(\mathbf{x}_i, \mathbf{x}_j)$, and the training labels and classifier weights as m -dimensional column vectors: $\mathbf{y} = (y_1, \dots, y_m)^T$, $\boldsymbol{\beta} = (\beta_1, \dots, \beta_m)^T$. Then we can re-express the optimisation problem as the following quadratic program:

$$\begin{aligned} & \min_{\boldsymbol{\beta}} \frac{1}{2} \boldsymbol{\beta}^T (\mathbf{y}^T \mathbf{K} \mathbf{y}) \boldsymbol{\beta} + \mathbf{q}^T \boldsymbol{\beta} \\ \text{subject to } & \mathbf{G}(\boldsymbol{\beta} \oplus \boldsymbol{\beta}) \leq \mathbf{h} \\ & \mathbf{y}^T \boldsymbol{\beta} = \mathbf{0}, \end{aligned} \quad (\text{S64})$$

where vector \mathbf{q} is a m -dimensional vector of -1 s, i.e. $\mathbf{q} = (-1, \dots, -1)^T$; matrix \mathbf{G} is a direct sum of the $m \times m$ identity matrix and its additive inverse, i.e. $\mathbf{G} = \mathbf{I}_m \oplus (-\mathbf{I}_m)$; and vector \mathbf{h} is a $2m$ -dimensional vector where the first m elements are C and the last m elements are 0 , i.e. $\mathbf{h} = (C, \dots, C, 0, \dots, 0)^T$. We then define a correction bias term b , given by

$$b = \frac{1}{m} \sum_{j=1}^m \left(y_j - \sum_{i=1}^m \beta_i y_i K(\mathbf{x}_j, \mathbf{x}_i) \right). \quad (\text{S65})$$

In all three classification tasks shown in the main text, we train the classifier with $m = 100$ training data vectors and we set the slack constant to $C = 0.8$. After we measure the overlap matrix \mathbf{K} , we solve the quadratic program using the CVXOPT package in Python [70].

Finally, for unseen new data \mathbf{x} , we compute its kernel function with the training dataset and compute its label by

$$\hat{y}(\mathbf{x}) = \text{sign} \left(\sum_{i=1}^m \beta_i y_i K(\mathbf{x}, \mathbf{x}_i) + b \right). \quad (\text{S66})$$

Practically, the β_i coefficients are non-zero only for a subset of the training data. The data vectors corresponding to non-zero β_i are called *support vectors* as they lie on the decision boundary of the hyperplane. The kernel function only needs to be evaluated against this subset of support vectors.

The quantum datasets used in our experiments are firstly generated in the parameter space of $\boldsymbol{\theta}$, i.e., the phases of the quantum states, while the amplitudes A_i in Equation S50 serve as hyperparameters. Through the scikit-learn package in python [71], we generate three types of datasets: separate, spherical and overlapping. Each dataset contains 100 training and 100 testing data vectors with proper parameter ranges. We check these datasets by running classical SVM algorithm, in which the kernels are simulated using different choices of $\{A_i\}_{i=0}^3$. Further, we optimize the hyperparameters to find the set $\{A_i\}_{i=0}^3$ in Equation S50 that yields optimal simulated classification accuracies of 100%, 100% and 97% for separate, spherical and overlapping datasets, respectively.

SVII. ONLINE LEARNING BY SIMULTANEOUS PERTURBATION STOCHASTIC APPROXIMATION

In our work we implemented an online learning protocol by simultaneous perturbation stochastic approximation (SPSA) algorithm [41, 56]. In this protocol, the unknown target state $|\psi(\mathbf{x}^{(t)})\rangle$, determined by encoded phases $\mathbf{x}^{(t)} = [\theta_1^{(t)}, \theta_2^{(t)}, \theta_3^{(t)}]$, is prepared on one of the two qudits. Then, we iteratively update the phase of the other qudit, $|\psi(\boldsymbol{\theta})\rangle$, to maximise the overlap between the two qudits. When the overlap approaches unity, then the second qudit approximately recovers the target state $|\psi(\mathbf{x}^{(t)})\rangle$ that we wish to learn. We define the cost function as

$$c(\boldsymbol{\theta}) = 1 - \left| \langle \psi(\mathbf{x}^{(t)}) | \psi(\boldsymbol{\theta}) \rangle \right|^2. \quad (\text{S67})$$

In the 0-th iteration, we pick an initial guess $\boldsymbol{\theta}^{(0)} = [\theta_1^{(0)}, \theta_2^{(0)}, \theta_3^{(0)}]$, where each $\theta_i^{(0)}$ is randomly initialised between 0 and 2π . In the k -th iteration, we generate a random perturbation vector $\boldsymbol{\Delta}^{(k)} \in \{\pm 1\}^{\otimes 3}$, where each component can

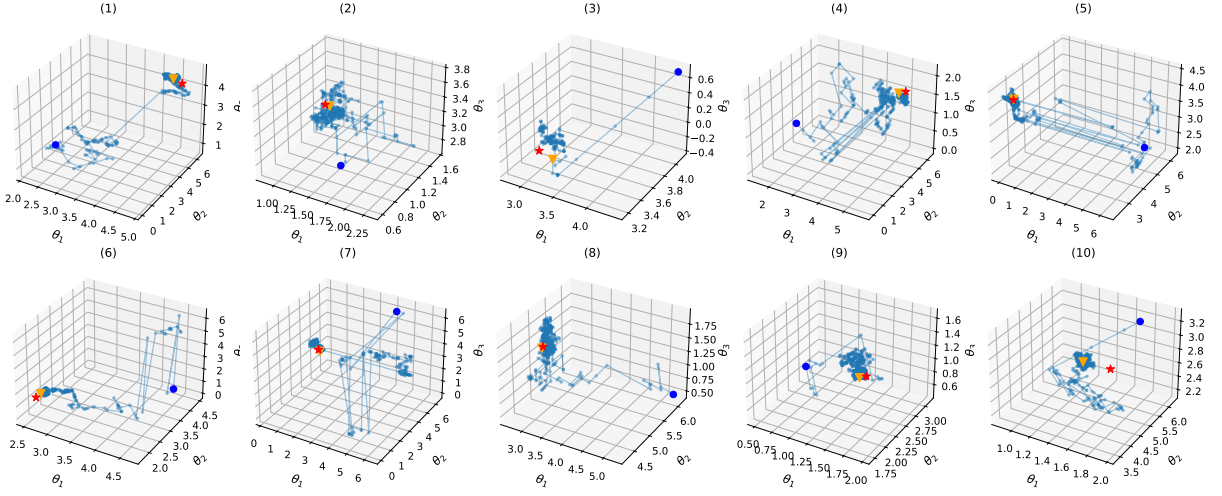


FIG. S5. The optimisation results for 10 randomly selected target phases. Each panel represents one experiment. Data shown for $N = 100$ samples per overlap measurement. The red star represents the phase $\mathbf{x}^{(t)}$ of the target state. The blue circle represents the initial guess, $\boldsymbol{\theta}^{(0)}$. The orange triangle represents the final guess after 500 iterations of the SPSA algorithm.

be ± 1 with equal outcome (i.e. follows the Bernoulli distribution). We evaluate the cost function at the simultaneous perturbation around the current phase values, $\boldsymbol{\theta}^{(k)}$: $c(\boldsymbol{\theta}^{(k)} \pm \Delta^{(k)} t^{(k)})$, where $t^{(k)}$ is a perturbation coefficient we will define later. Operationally, this means encoding the phases $\boldsymbol{\theta}^{(k)} \pm \Delta^{(k)} t^{(k)}$ and measuring the overlaps respectively. We repeat the experiments for $N = 100, 1000$ and 10000 samples per overlap measurement, as shown in the main text.

The simultaneous perturbation allows us to approximate the local gradient at $\boldsymbol{\theta}^{(k)}$ to be:

$$\mathbf{g}(\boldsymbol{\theta}^{(k)}) = \frac{c(\boldsymbol{\theta}^{(k)} + \Delta^{(k)} t^{(k)}) - c(\boldsymbol{\theta}^{(k)} - \Delta^{(k)} t^{(k)})}{2t^{(k)} \Delta^{(k)}}. \quad (\text{S68})$$

We then update the phase parameters for the $k + 1$ -th iteration to be

$$\boldsymbol{\theta}^{(k+1)} = \boldsymbol{\theta}^{(k)} - a^{(k)} \mathbf{g}(\boldsymbol{\theta}^{(k)}), \quad (\text{S69})$$

where $a^{(k)}$ is a gain coefficient that determines how much we update the phase parameters at each iteration.

The perturbation and gain coefficients decay with iterations, and are defined as

$$a^{(k)} = \frac{a}{(A + k + 1)^\alpha}, \quad t^{(k)} = \frac{t}{(k + 1)^\gamma}. \quad (\text{S70})$$

The coefficients α, γ govern the rate of decay for both $a^{(k)}$ and $t^{(k)}$. Following the guidelines of Ref. [56], we choose $\alpha = 0.602, \gamma = 0.101$ respectively. The coefficient A is a ‘stability constant’ that allows for larger a coefficient in the numerator of $a^{(k)}$ while ensuring stability in early iterations. Ref. [56] recommends to choose a value of A that is much less than the maximum number of iterations allowed. In our experiments, we run the protocol for 500 iterations, and choose $A = 10$. The a coefficient determines the step size of each iteration. Heuristically, we found that setting $a = 1.6$ gives a good convergence rate for our experiments.

Finally, the t coefficient determines the magnitude of the perturbation at each step. Ref. [56] recommends a selection of t that is approximately the standard deviation of the measurement noise, so that the perturbed cost function values are noise-robust. We follow this guideline. At the start of the 0-th iteration, we evaluate the initial cost function, $c(\boldsymbol{\theta}^{(0)})$, five times and set t to be twice the standard deviation of the measurement results.

We repeat the optimisation routine for ten randomly selected target phases, corresponding to ten different target states. The results are summarised in the main text as well as Fig. S5.